Comprehensive analysis of earthquake source spectra in southern California

Peter M. Shearer,[1] Germán A. Prieto,[1] and Egill Hauksson[2]

Received 4 August 2005; revised 20 December 2005; accepted 16 February 2006; published 13 June 2006.

[1] We compute and analyze *P* wave spectra from earthquakes in southern California between 1989 and 2001 using a method that isolates source-, receiver-, and path-dependent terms. We correct observed source spectra for attenuation using both fixed and spatially varying empirical Green's function methods. Estimated Brune-type stress drops for over 60,000 M_L = 1.5 to 3.1 earthquakes range from 0.2 to 20 MPa with no dependence on moment or local *b* value. Median computed stress drop increases with depth in the upper crust, from about 0.6 MPa at the surface to about 2.2 MPa at 8 km, where it levels off and remains nearly constant in the midcrust down to about 20 km. However, the results at shallow depths could also be explained as reduced rupture velocities near the surface rather than a change in stress drop. Spatially coherent variations in median stress drop are observed, with generally low values for the Imperial Valley and Northridge aftershocks and higher values for the eastern Transverse ranges and the north end of the San Jacinto fault. We find no correlation between observed stress drop and distance from the San Andreas and other major faults. Significant along-strike variations in stress drop exist for aftershocks of the 1992 Landers earthquake, which may correlate with differences in main shock slip.

Citation: Shearer, P. M., G. A. Prieto, and E. Hauksson (2006), Comprehensive analysis of earthquake source spectra in southern California, *J. Geophys. Res.*, *111*, B06303, doi:10.1029/2005JB003979.

1. Introduction

[2] Most earthquakes are inaccessible to direct observation and our knowledge of their source properties relies primarily on records of their radiated seismic waves. Many fundamental earthquake properties can be measured from the spectral content of *P* and *S* wave arrivals. For example, moment, M_0, is computed from the low-frequency limit of the displacement spectra and radiated seismic energy, E_S, is computed from integrated velocity spectra. Stress drop, $\Delta\sigma$, can be computed through estimates of fault area constrained by the spectral corner frequency (inversely related to the pulse width).

[3] An issue of continuing interest has been earthquake scaling and whether earthquakes are self-similar as proposed by *Aki* [1967] such that stress drop and apparent stress (proportional to E_S/M_0) are constant with respect to moment. Resolution of this question has been hampered by the large scatter in observed stress drops compared to the possible deviations in stress drop from self-similarity. For small earthquakes, corrections for attenuation and other path effects are particularly important, which has led to the development of empirical Green's function (EGF) methods [e.g., *Mueller*, 1985; *Hough*, 1997].

[4] Observed stress drops for crustal earthquakes as estimated using corner frequency methods vary from about 0.2 to 20 MPa [e.g., *Tucker and Brune*, 1973; *Thatcher and Hanks*, 1973; *Mori and Frankel*, 1990; *Abercrombie*, 1995; *Hough and Dreger*, 1995; *Jin et al.*, 2000; *Bindi et al.*, 2001] but are generally much less than the 50 to 150 MPa absolute shear stresses predicted for crustal earthquakes from Byerlee's law and rock friction coefficients measured in laboratory experiments. The relationship, if any, between stress drop and absolute stress is part of an enduring controversy concerning the strength of crustal faults (for opposing views, see *Scholz* [2000] and *Brune and Thatcher* [2002]).

[5] Another question is whether variations in observed stress drops can be related to differences in tectonic setting. From teleseismic studies, there is some evidence that plate boundary (interplate) earthquakes have lower average stress drops than midplate (intraplate) earthquakes [e.g., *Kanamori and Anderson*, 1975; *Scholz et al.*, 1986; *Zhuo and Kanamori*, 1987]. Some studies also suggest that the average stress drop and apparent stress for reverse faulting earthquakes are larger than that of strike-slip and normal fault events [e.g., *Cocco and Rovelli*, 1989; *McGarr and Fletcher*, 2002]. Results from southern California, however, have shown a wide range of stress drops with limited correlation to tectonics [*Thatcher and Hanks*, 1973; *Mori and Frankel*, 1990; *Kanamori et al.*, 1993; *Jones and Helmberger*, 1996, 1998].

[1] Institute of Geophysics and Planetary Physics, Scripps Institution of Oceanography, University of California, San Diego, La Jolla, California, USA.

[2] Seismological Laboratory, California Institute of Technology, Pasadena, California, USA.

0148-0227/06/2005JB003979$09.00

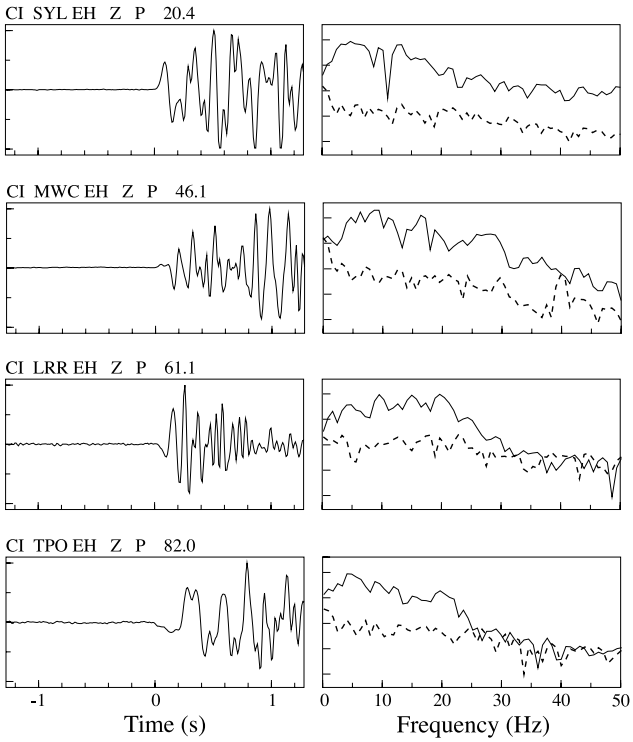

Figure 1. Examples of seismograms and computed spectra from four stations recording an $M_L = 2.5$ earthquake on 2 September 1995 (SCSN Cusp ID 3229009). (left) Time series in relative amplitude, with zero time marking the division between 1.28 s noise and signal windows. (right) Log displacement spectra for both the signal (solid line) and noise (dashed line). Each *y* axis tic mark is a factor of 10 in spectral amplitude. Source-receiver distances range from 20.4 to 82.0 km.

[6] As noted by *Brune et al.* [1979] and *Hough* [1996], one difficulty in comparing results among studies is that analyses are often done using different modeling assumptions. Differences may include the assumed rupture velocity, high-frequency falloff rate (i.e., ω^{-2}, ω^{-3}, etc.), source geometry, and corrections for attenuation. Because stress drop estimates vary as the cube of the computed source dimension, even small variations in these parameters can produce significant changes in computed stress drops. Our goal in this paper is to use a consistent approach to analyze spectra from earthquakes in southern California to identify variations in source properties. We exploit the large number of source-receiver pairs to solve for empirical source, receiver and propagation path terms, and to estimate stress drop using the *Brune* [1970] approach. Our results for over 60,000 earthquakes of M_L 1.5 to 3.1 indicate a large range of inferred stress drops with spatially coherent variations in average stress drop, but with no general correlation with faults or other tectonic features.

2. Data Processing

[7] The Southern California Seismic Network (SCSN) has several hundred stations and records about 12,000 to 35,000 earthquakes each year. Recently, we began storing seismograms from all archived events in an online RAID system that provides rapid and random access to the data [*Hauksson and Shearer*, 2005]. Here we examine data for over 230,000 events between 1989 and 2001, a period when the network was relatively stable in terms of instrumentation, consisting mainly of short-period vertical component sensors. Spectra are computed as follows: For each seismogram we pick the *P* and *S* arrivals. This is done using the operator pick, if available, or using the output of an automatic picking algorithm for a window around the predicted arrival time (based on the catalog event location and a one-dimensional velocity model). Traces are resampled to a uniform 100 Hz sample rate. Spectra are computed using a multitaper algorithm [e.g., *Park et al.*, 1987] for 1.28 s noise and signal windows immediately before and after the pick time. We compute results for all available channels and components for both *P* and *S*, including rotation of the horizontals (if present) into transverse and radial records. However, in this study we analyze only *P* waves from the vertical EH (short-period) component. Both signal and preevent noise spectra are corrected to displacement and stored in a special binary format. We note that these records generally clip for $M_L \geq 3.5$ earthquakes.

[8] Next, we apply a signal-to-noise (STN) cutoff to the spectra, requiring that the STN amplitude ratio be at least 5 for three separate bands of 5 to 10 Hz, 10 to 15 Hz, and 15 to 20 Hz. The resulting data consist of 1.1 million *P* spectra from 235,128 events, recorded at 354 stations. Examples of these spectra are plotted in Figure 1 for an M_L = 2.5 earthquake. Although the spectra are shown plotted between 0 and 50 Hz, our analysis will concentrate on the 2 to 20 Hz band, which generally has the highest average STN ratios. Next, we process the spectra in order to isolate source, receiver and propagation path effects. This is an important step because individual spectra tend to be irregular in shape and difficult to fit robustly with theoretical models. However, by stacking and analyzing thousands of spectra it is possible to obtain more consistent results.

[9] The basic approach is illustrated in Figure 2 and is similar to methods used by *Andrews* [1986], *Boatwright et al.* [1991], *Warren and Shearer* [2000, 2002], and *Prieto et al.* [2004]. Each observed displacement spectrum $d_{ij}(f)$ from source *i* and receiver *j* is a product of a source term e_i (which includes the source spectrum and near-source attenuation), a near-receiver term s_j (which includes any uncor-

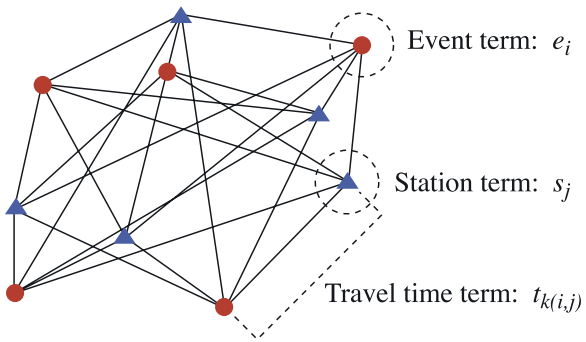

Figure 2. A cartoon showing how measured spectra can be modeled as a product of event, station, and traveltime-dependent terms.

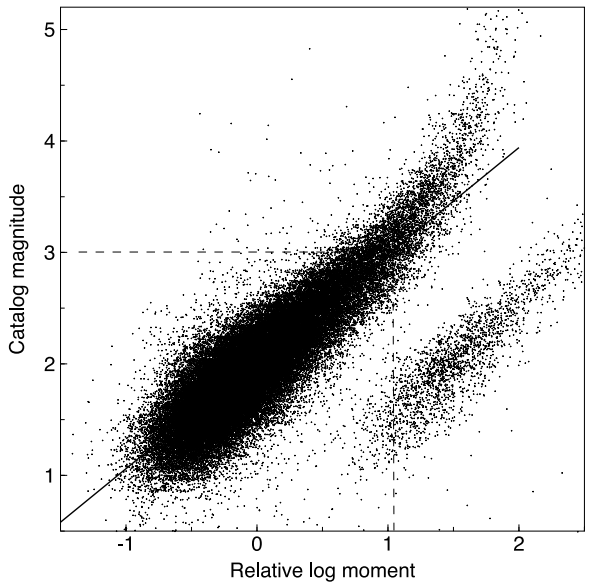

Figure 3. Relative moment M_0 obtained from the low-frequency amplitude of the stacked source spectra versus catalog magnitude M_L. The solid line has a slope of 0.96 and shows the fit to the main data trend for relative log moments between −1.5 and 1. The dashed lines show the relative moment assumed to correspond to M_W = 3 (see text). The separate population of points to the right probably results from differences in the network gain and are discarded.

rected part of the instrument response, the site response and the near-receiver attenuation), and a traveltime-dependent term t_k (which includes the effects of geometrical spreading and attenuation along the ray path). In the log domain, this product becomes a sum:

$$d_{ij} = e_i + s_j + t_{k(i,j)} + r_{ij} \quad (1)$$

where r_{ij} is the residual for path ij. We parameterize t in terms of the predicted P traveltime between the source and receiver, using the event locations and velocity model from *Shearer et al.* [2005]. This accounts for both the event depth and the source receiver distance. The traveltime term t is discretized by its index k at 1 s increments in traveltime.

[10] Because each station records multiple events and each event is recorded by multiple stations, this is an overdetermined problem. We solve (1) using a robust, iterative, least squares method in which we sequentially solve individually for the terms t_k, s_j, and e_i, keeping the other terms fixed at each stage. We suppress outliers by assigning $L1$ norm weights to misfit residuals greater than 0.2 s (or less than −0.2 s). This weighting scheme is necessary to ensure robustness with respect to a small number of spectra with large excursions compared to the bulk of the data. In practice we found that the method converged rapidly to a stable solution after a few iterations.

[11] Radiation pattern differences are not included in equation (1) and would be difficult to include in our processing because they are not generally available for the smaller magnitude events. By using multiple stations for each source, however, radiation pattern effects will tend to average out. Note that this method resolves only differences in the relative shapes of the spectra. Without additional modeling assumptions, it cannot, for example, resolve how much of the spectral falloff is due to source effects and how much is due to attenuation common to all paths. The advantage of the method, however, is that it identifies and removes anomalies that are specific to certain sources or receivers. Because there may be difficulties in obtaining reliable and accurate instrument response functions for many of the stations in the archive, this is an important processing step that provides a way to correct for some of these problems.

[12] Our focus in this paper will be on the stacked source spectra, e_i, which we ultimately will use to estimate the moment and corner frequency of each event. At this stage, however, the source spectra only contain relative information among the different events. To estimate absolute spectra from our source stacks, we will use the local magnitude M_L to obtain the scaling factor necessary to convert our relative moment estimates to absolute moment and we will use an empirical Green's function approach to correct the spectral shapes for attenuation and other path effects.

2.1. Calibration to Absolute Moment

[13] The low-frequency amplitudes of our source displacement spectra should be proportional to seismic moment, M_0. Computing seismic moment directly from source spectra requires well-calibrated instruments and the ability to accurately correct for geometrical spreading and other path effects. We do not attempt such a calculation here; rather, following *Prieto et al.* [2004], we use the assigned SCSN local magnitude to provide an absolute measure of the size of our events. We estimate relative moment from our spectra from the mean amplitude of points 3 to 5 of each source stack (1.6 to 3.1 Hz, well below the corner frequency of these events). We do not use the first two spectral points (0 and 0.8 Hz) because the instrument response does not extend to zero frequency and the 0.8 Hz point has lower signal-to-noise than the next three points.

[14] Figure 3 plots relative log moment versus local magnitude for 68,803 events of $0.5 \leq M_L \leq 5.2$ with five or more stations contributing spectra. The bulk of the data are highly correlated but a small number of events exhibit a large shift in relative moment compared to the other events. These events all occurred during short time intervals within the 12 year span of our total data set, during which times it appears the network gain differed by a factor of about 100 compared to the normal gain setting. We have not yet determined if this is a problem with the SCSN network calibration or if it occurred somewhere in the creation of our online database. In any case, these events are only 3.3% of the total data, and we simply discard them for the analysis presented here, in which we assume that the station term, s_j, is constant with respect to time. We also note the linear trend of magnitude versus relative moment breaks down for earthquakes larger than about M 3; presumably, our observed amplitudes for these events are reduced due to clipping and/or a shift to corner frequencies near or below our 1.6 to 3.1 Hz measurement band.

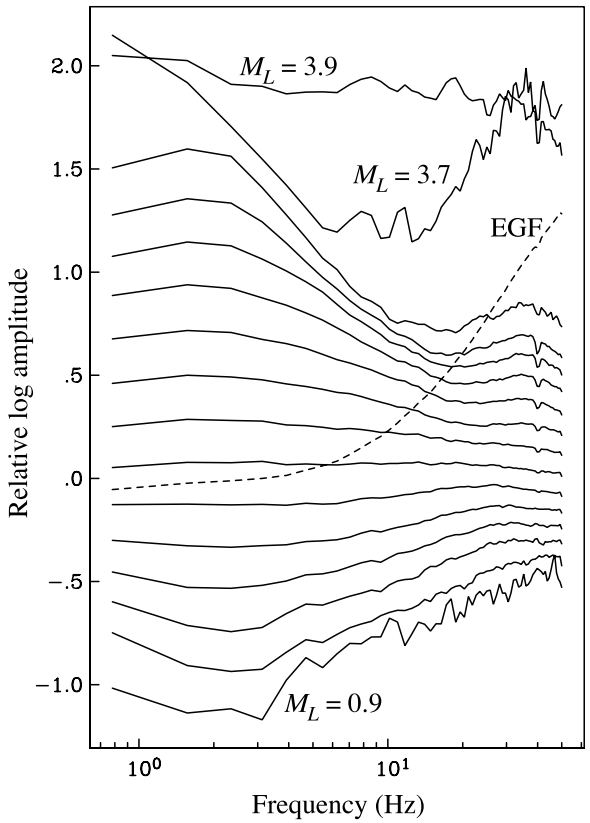

Figure 4. Log amplitude of source spectral terms, binned in increments of 0.2 in estimated local magnitude M_L. The dashed line shows the empirical Green's function (EGF) computed for these spectra; the EGF-corrected spectra plotted in Figure 5 result from subtracting the EGF log spectrum from the spectra shown here.

[15] The line shows the best $L1$ norm fit between our relative moment estimates and observed catalog magnitude for relative moments between −1.5 and 1. The best fitting slope is 0.96, significantly more than the slope of 2/3 predicted by assuming $M_L = M_W$ and defining M_W using the *Kanamori* [1977] relation

$$M_W = \frac{2}{3}\log_{10} M_0 - 10.7 \qquad (2)$$

where M_0 is the moment measured in dyn cm. We note that the scaling factor between $\log(M_0)$ and M_L has varied somewhat in previous studies, particularly those that span a wide magnitude range [e.g., *Hanks and Boore*, 1984]. Results at magnitudes comparable to our study have varied between about 2/3 and 1, with *Bakun* [1984] obtaining 0.83 for $1.5 \le M_L \le 3.5$, *Abercrombie* [1996] getting 1.0 for $M_L < 3.7$, *Ben-Zion and Zhu* [2002] obtaining 1.0 for $M_L < 3$, and *Prieto et al.* [2004] finding ~2/3 for $1.8 \le M_L \le 3.4$.

[16] To calibrate our results, we assume that $M_L = M_W$ at $M_L = 3.0$ and use our relative moment estimates to compute M_W using equation (2) for other size events. We do not use the assigned local magnitudes for individual events to estimate moment. Because of the difference between our observed scaling and the 2/3 factor in (2), this implies that $M_L = 2.0$ events correspond to $M_W = 2.31$ and $M_L = 1.0$ events correspond to $M_W = 1.61$. This follows directly from Figure 3; the range in observed M_0 as M_L varies from 1 to 3 is too small to be compatible with the 2/3 factor in equation (2). Note that the choice of which magnitude to match M_L and M_W determines the overall estimated moment of all of our events. We chose the $M_L = 3$ point because it seems more likely that the local magnitude scale would be calibrated with M_W at larger magnitudes, closer in size to the bigger earthquakes for which moment is routinely calculated.

[17] This calibration using the catalog magnitudes is how we translate our observed relative moments into M_0 and M_W. However, because there is some uncertainty in the scaling between M_L and M_W, our absolute moment values are approximate and are not as well constrained as the relative moments among the events.

2.2. Relative Source Spectral Shapes

[18] To examine variations in the average source spectra as a function of event size, we average the spectra within bins of 0.2 units in estimated local magnitude. As before, we only use source spectra obtained from five or more individual station spectra. We use computed local magnitude (rather than catalog M_L) as estimated from our observed relative moment and the linear fit shown in Figure 3. Thus our binning scheme is very close to 0.2 increments in log moment (because the slope in Figure 3 is close to unity). Results are plotted in Figure 4 for 16 bins centered on $M_L = 0.9$ to 3.9. The number of source spectra within each bin falls off for both the smallest and largest magnitudes. There are only 15 sources contributing to the $M_L = 0.9$ bin compared to 140 for $M_L = 1.1$ and 885 for $M_L = 1.3$. Only two source spectra contribute to the $M_L = 3.9$ bin and three to the $M_L = 3.7$ bin, compared to 42 in the $M_L = 3.5$ bin and 195 in the $M_L = 3.3$ bin. The bins with few data have irregular shaped spectra compared to the generally smoother results obtained from stacking larger numbers of sources. In addition, the two larger event bins likely suffer from clipped data. For these reasons, we use only the M_L = 1.5 to 3.1 results in our subsequent analyses.

[19] As discussed above, our moment estimates are derived from the average amplitude of the 1.6, 2.3 and 3.1 Hz points in the spectra. This is why the stacked spectra plotted in Figure 4 are approximately evenly spaced over that frequency interval. Our iterative approach to solving equation (1) has the effect of setting the mean source spectra to zero. Thus the source spectra at this point in our analysis only contain relative information among the different events. The positive slopes of the small event spectra near 10 Hz, compared to the negative slopes of the large event spectra, are caused by the higher corner frequencies of the smaller events.

2.3. Single EGF Method

[20] The traditional empirical Green's function (EGF) approach [e.g., *Mueller*, 1985; *Frankel et al.*, 1986] corrects the spectrum of a target earthquake for Q and other path effects by using the observed spectra of one or more nearby earthquakes that are significantly smaller than the target. In its simplest form the method assumes that these smaller

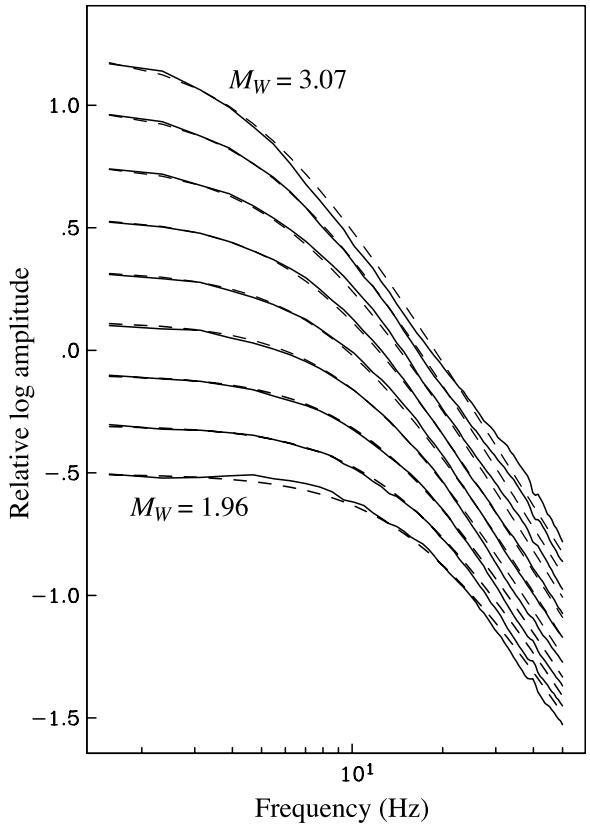

Figure 5. EGF-corrected stacked source spectra (solid lines) compared to predictions of a constant stress drop ($\Delta\sigma$ = 1.6 MPa) ω^{-2} source model (dashed lines). Estimated M_W varies at even intervals between 1.96 and 3.07.

events have sufficiently high corner frequencies that their spectra are flat (i.e., they provide the delta function Earth response). In the frequency domain the method can by implemented simply by subtracting the average log spectra of the smaller events from the larger event. In practice, random irregularities in the spectra of the smaller events often lead to complications in the appearance of the corrected spectra. These complications can be reduced by applying water level deconvolution or other smoothness constraints. Alternatively, the spectra can be smoothed at the outset by stacking many individual source spectra.

[21] One way to apply the EGF method to the binned spectra in Figure 4 would be to subtract the smallest moment bin containing a smooth spectra from all of the other binned log spectra. This was the approach used by *Prieto et al.* [2004] to analyze an event cluster recorded by the Anza seismic network in southern California. However, there are two disadvantages to this method. First, the results are only useful for size bins at least one magnitude greater than the EGF bin and thus results for many events must be discarded. Second, the EGF correction is only approximate because the spectrum from even the smallest magnitude bin will have a finite corner frequency and will have some falloff even well below the corner frequency.

[22] To address these difficulties, we have developed a method that simultaneously fits the binned source spectra with a theoretical source model and solves for an EGF. Our approach is similar to previous methods for multiple-empirical Green's function analysis [e.g., *Boatwright et al.*, 1991; *Humphrey and Anderson*, 1994; *Hough*, 1997] except that we group and stack the event spectra within bins of similar moment before computing the EGF. We assume our displacement spectra have the form [e.g., *Brune*, 1970]

$$u(f) = \frac{\Omega_0}{1 + (f/f_c)^n} \tag{3}$$

where Ω_0 is the long-period amplitude (proportional to moment), n is the assumed high-frequency falloff rate (i.e., $n = 2$ for ω^{-2} models), and f_c is the corner frequency. We assume a source model [*Madariaga*, 1976; *Abercrombie*, 1995] in which the corner frequency is related to the stress drop by

$$f_c = \frac{0.42\beta}{(M_0/\Delta\sigma)^{1/3}} \tag{4}$$

where β is the shear velocity, M_0 is the moment, and $\Delta\sigma$ is the stress drop. We assume a constant shear velocity of 3.464 km/s ($=6/\sqrt{3}$) throughout our analyses.

[23] It should be noted that equation (4) assumes circular rupture and a constant rupture velocity of 0.9β. For convenience throughout most of this paper, we will use the term "stress drop" to refer to our Brune-type $\Delta\sigma$ estimates as obtained by using equation (4), but it should be understood that our estimates are not necessarily the true static stress drops for the earthquakes. The relationship between the Brune-type stress drop (sometimes also referred to as dynamic stress drop or effective stress) and static stress drop has been the subject of some discussion [e.g., *Andrews*, 1986; *Snoke*, 1987; *Hough*, 1996].

[24] We chose to model only the smoothest, most reliable stacks shown in Figure 4, the nine bins between M_L = 1.5 and 3.1 (corresponding to M_W = 1.96 to 3.07, as discussed above). We also fit only between 2 and 20 Hz, where we have the best signal-to-noise. Because Ω_0 and M_0 are obtained from the long-period part of the spectra (see above), the only two unknowns in this source model are n and $\Delta\sigma$. We experimented with allowing these parameters to vary as a function of moment, but found that a good fit to the spectra could be obtained using $n = 2$ (the ω^{-2} model) and a single fixed value of stress drop. In this case, the fitting procedure is relatively simple:

[25] 1. Loop over a range of possible values of $\Delta\sigma$.

[26] 2. For each value of $\Delta\sigma$, compute theoretical source spectra for each of the nine observed spectra, using the appropriate value of M_0 in each case.

[27] 3. Shift the theoretical log spectra to agree with the observed log spectral amplitude at long periods.

[28] 4. Estimate the EGF by averaging the differences between the observed and theoretical log spectra at each frequency point. Note that there is a single EGF spectrum for all of the different source bins.

[29] 5. Compute the RMS misfit over the 2 to 20 Hz band from the difference between the theoretical spectra and the EGF-corrected observed spectra.

[30] 6. Repeat to identify the best fitting value of $\Delta\sigma$.

[31] The method yields $\Delta\sigma$ = 1.60 MPa and corner frequencies ranging from 4.8 to 17 Hz. Figure 5 plots the fit to the EGF-corrected data stacks, while Figure 4 shows the EGF itself. The data curves in Figure 5 are the result of subtracting the EGF from each of the stacked source log spectra in Figure 4. The smoothness of this EGF suggests that the method is not introducing spurious structure into the corrected spectra. The good overall agreement at 2 to 20 Hz between the observed and theoretical spectra in Figure 5 indicates that a simple, constant stress drop model can explain the main features in the data stacks. Above 20 Hz, the theoretical model systematically overpredicts amplitudes for the smaller events and underpredicts amplitudes for the larger events (the average residual at each frequency point is always zero because of the way the EGF is calculated). This misfit is likely caused by the reduced signal-to-noise above 20 Hz.

[32] A constant stress drop model is consistent with self-similarity in earthquake scaling between large and small earthquakes. This implies that the spectra plotted in Figure 5 all have similar shapes (on a log-log plot) but are shifted along an f^{-3} line [e.g., *Aki*, 1967; *Prieto et al.*, 2004]. We experimented with permitting $\Delta\sigma$ to have different values in fitting the nine spectra plotted in Figure 5, but did not achieve a significantly better fit than the constant stress drop model. Furthermore, the nine individual $\Delta\sigma$ values obtained were close to 1.60 MPa (ranging from 1.33 to 1.77 MPa) and did not vary systematically with moment. This is consistent with results for individual events (to be discussed later), which show constant median stress drop as a function of moment.

[33] We also experimented with allowing n to vary in the fitting procedure and found small departures from n = 2. However, because this did not significantly improve the overall fit to the observed spectra, for simplicity we assume n = 2 throughout this study. Finally we note that the success of our approach in this section depends upon there being a significant range of event moment and corner frequency. If all of the events were the same size, then there would be an unresolvable tradeoff between the model predicted spectrum and the EGF. The procedure is stable only when a single EGF is applied to a variety of different spectral shapes.

[34] Another earthquake source parameter that is often computed from spectra is apparent stress, σ_a, which is a measure of the difference between the average loading stress, $\overline{\sigma}$, and the resisting stress, σ_r, during an earthquake. Apparent stress is a dynamic property of earthquakes, which can be computed from seismic observations using $\sigma_a = \mu E_s/M_0$ where E_s is the radiated seismic energy, μ is the shear modulus and M_0 is the moment. E_s can be computed from the integrated observed P and S velocity spectra by applying corrections for path effects from the source. In principle, an advantage of estimating apparent stress compared to stress drop from seismic data is that no source model assumptions are required (i.e., no fitting to a corner frequency model, no assumed rupture velocity, etc.). However, in practice large bandwidth is required as well as accurate corrections for attenuation and source directivity. It would be difficult to reliably estimate apparent stress in our study because of the 20 Hz upper limit of our good signal-to-noise data and the lack of S wave results (which contain most of the radiated energy).

[35] Stress drop and apparent stress are not independent parameters. An earthquake of fixed moment that radiates more high frequencies will have both increased stress drop and apparent stress compared to an earthquake with less high-frequency radiation. Indeed, given a theoretical model of the earthquake source spectrum, $\Delta\sigma$ and σ_a are proportional to each other and will obey the same scaling [e.g., *Savage and Wood*, 1971; *Andrews*, 1986; *Di Bona and Rovelli*, 1988; *Singh and Ordaz*, 1994; *Hough*, 1996; *Beeler et al.*, 2003; *Kanamori and Rivera*, 2004]. Our results indicate that the ω^{-2} model provides a good fit to the average spectral properties of southern California earthquakes, at least over the M_L = 1.5 to 3 range of our data, suggesting that a simple scaling may exist between stress drop and apparent stress. However, this result does not necessarily hold for individual earthquakes within each data stack because they may have source spectra that deviate from the ω^{-2} model.

2.4. Attenuation Modeling

[36] Traditional EGF analysis is done separately for each target event using nearby smaller earthquakes. Because the source-receiver paths for the events are very similar, the EGF isolates the source spectrum by removing the path and receiver response, including the effects of attenuation. In our analysis, we are combining data from a wide variety of source-receiver paths and distances across southern California. Thus the validity of our approach of using a single EGF to calibrate all of our source spectra depends upon how effectively the station terms, s_j, and traveltime-dependent terms, $t_{k(i,j)}$, in equation (1) correct for attenuation and differences in near-receiver response. One test of our method is whether our computed $t_{k(i,j)}$ spectra are consistent with a reasonable Q_α model for southern California.

[37] Each of the terms on the right side of equation (1) is uncertain with respect to a constant log spectrum that could be added and subtracted from any pair of terms without changing their sum. The method described in section 2.3 removes this ambiguity from the source spectral terms, e_i, by solving for an EGF to be subtracted from every source log spectra. To continue satisfying equation (1), the source EGF must be added to either the traveltime or receiver terms; we choose to add it to the traveltime terms.

[38] Our approach in fitting a Q_α model to the traveltime spectral terms is similar to that used for the source EGF:

[39] 1. Loop over a range of possible values of Q_α. For simplicity we assume Q_α is constant, i.e., it does not vary with traveltime.

[40] 2. For each value of Q_α, compute theoretical source spectra for 20 traveltime-dependent spectral terms (computed at 1 s intervals, ranging from 0 to 20 s). Shift these log spectra to agree with the average amplitude of the observed spectra between 5 and 20 Hz. We perform this shift because we are only attempting to fit the slopes of the $t_{k(i,j)}$ spectra, not their absolute amplitudes, which are dependent upon geometrical spreading and other factors in addition to attenuation.

[41] 3. Estimate an empirical correction spectrum (which we term ECS) by averaging the differences between the

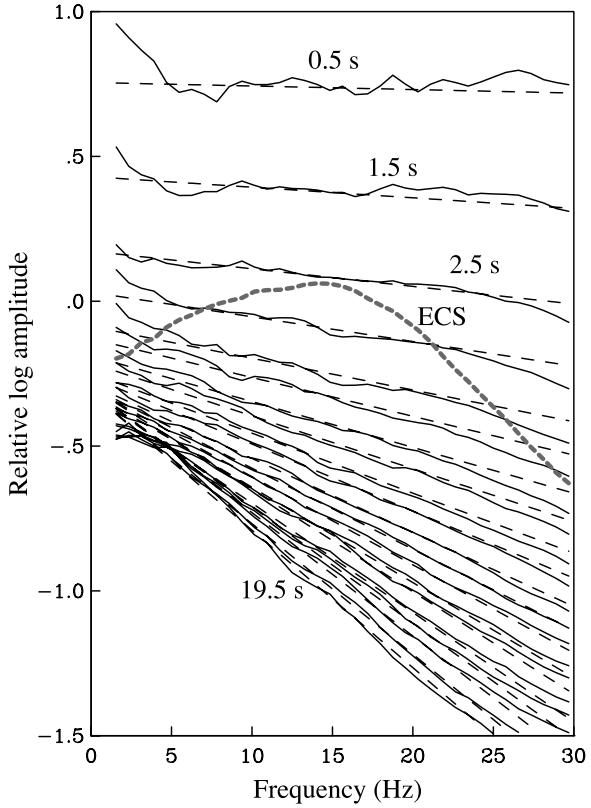

Figure 6. Source-receiver traveltime spectral terms at 1 s increments between 0.5 and 19.5 s compared to predictions of a $Q_\alpha = 560$ attenuation model. The dashed line shows the empirical correction spectrum (see text).

observed and theoretical log spectra at each frequency point. Note that there is a single ECS for all of the different $t_{k(i,j)}$.

[42] 4. Compute the RMS misfit over the 5 to 20 Hz band from the difference between the theoretical spectra and the ECS-corrected observed spectra.

[43] 5. Repeat to identify the best fitting value of Q_α.

[44] The method yields $Q_\alpha = 560$, in reasonable agreement with the attenuation values obtained by *Schlotterbeck and Abers* [2001] and *Hauksson and Shearer* [2005] for southern California crust. Figure 6 plots the fit to the ECS-corrected spectra and the ECS function itself. Linear rather than log frequency is plotted to emphasize the straight lines predicted by the uniform Q model. The t^* values range from 0.0009 s at 0.5 s to 0.035 s at 19.5 s. The data curves in Figure 6 are the result of subtracting the ECS from each of the $t_{k(i,j)}$ spectra. As in the case of the EGF function used to correct the source spectra, the smoothness of the ECS indicates that the method is not introducing spurious structure into the corrected spectra. The good overall agreement at 5 to 20 Hz between the observed and theoretical spectra in Figure 6 indicates that a simple, uniform Q model can explain the main features in the data stacks. Above 20 Hz the fit deteriorates, presumably due to increasing noise at these frequencies. Below 5 Hz, there is some mismatch, with the model underpredicting data amplitudes at small traveltimes and overpredicting data amplitudes at large traveltimes.

[45] Because attenuation is generally strongest in the near-surface below each station, the $Q_\alpha = 560$ model does not include all of the attenuation along the ray paths. However, effects of the low-Q structure in the shallow crust are absorbed into the receiver terms, s_j. To continue satisfying equation (1), we add the ECS to s_j to obtain our final set of receiver terms. These receiver terms, as well as the individual residual spectra for each source-receiver ray path, could be used to study Q structure across southern California. In this study, however, we continue to focus on the source spectra.

2.5. Single EGF Applied to Individual Events

[46] To obtain results for individual events, we subtract the EGF computed from the average spectra (binned by moment, see Figures 4 and 5), from the individual event spectral terms, e_i, to obtain estimates of the true source spectra. In principle, these are corrected for the dominant effects of attenuation and near-receiver response variations. Next, we find the best fitting corner frequency for each source, using equation (3) and compute the stress drop, $\Delta\sigma$, using equation (4). Requiring at least 5 stations recording each source, we obtain results for 65,664 events and a median stress drop of 1.57 MPa, in good agreement with the value of 1.60 MPa obtained by fitting the average spectra with a uniform stress drop. However, as shown in Figure 7, the individual event stress drops exhibit considerable variations, ranging from about 0.2 to 20 MPa. There are also spatially coherent patterns in average stress drop, with low stress drops seen in the Imperial Valley and Northridge aftershocks, and high stress drops seen at the north end of the San Jacinto fault. Aftershocks of the 1992 Landers earthquake exhibit considerable along-strike variations in $\Delta\sigma$ (these variations are difficult to see in the large-scale map of Figure 7; later plots will show this in more detail).

[47] These $\Delta\sigma$ values are specific to our assumed source model and would change under different modeling assumptions (e.g., if we had used the *Brune* [1970] model rather than *Madariaga* [1976] model, if the rupture velocity differed from 0.9β, or if our moment calibration was offset by some amount). Any of these effects would shift the median stress drop away from our value of 1.6 MPa. However, because we have applied a single method uniformly to all of the events, the relative sizes of the stress drops do not depend upon the details of the model. The variations in estimated stress drops reflect differences in the frequency content of our source spectra estimates; these differences are a robust feature in our analysis.

[48] Our source spectral estimates may, however, be biased by variations in near-source attenuation. Thus some of the stress drop variations seen in Figure 7 may be caused by lateral variations in Q_α at depth. This is more likely to be a factor in comparing large-scale differences among regions than differences among nearby events, which will have similar source-receiver ray paths. For example, high attenuation in the Imperial Valley might remove high frequencies from the source spectra and cause smaller corner frequency estimates and correspondingly lower stress drop estimates. However, the along-strike variations in $\Delta\sigma$ seen for Landers aftershocks occur at such short length scales

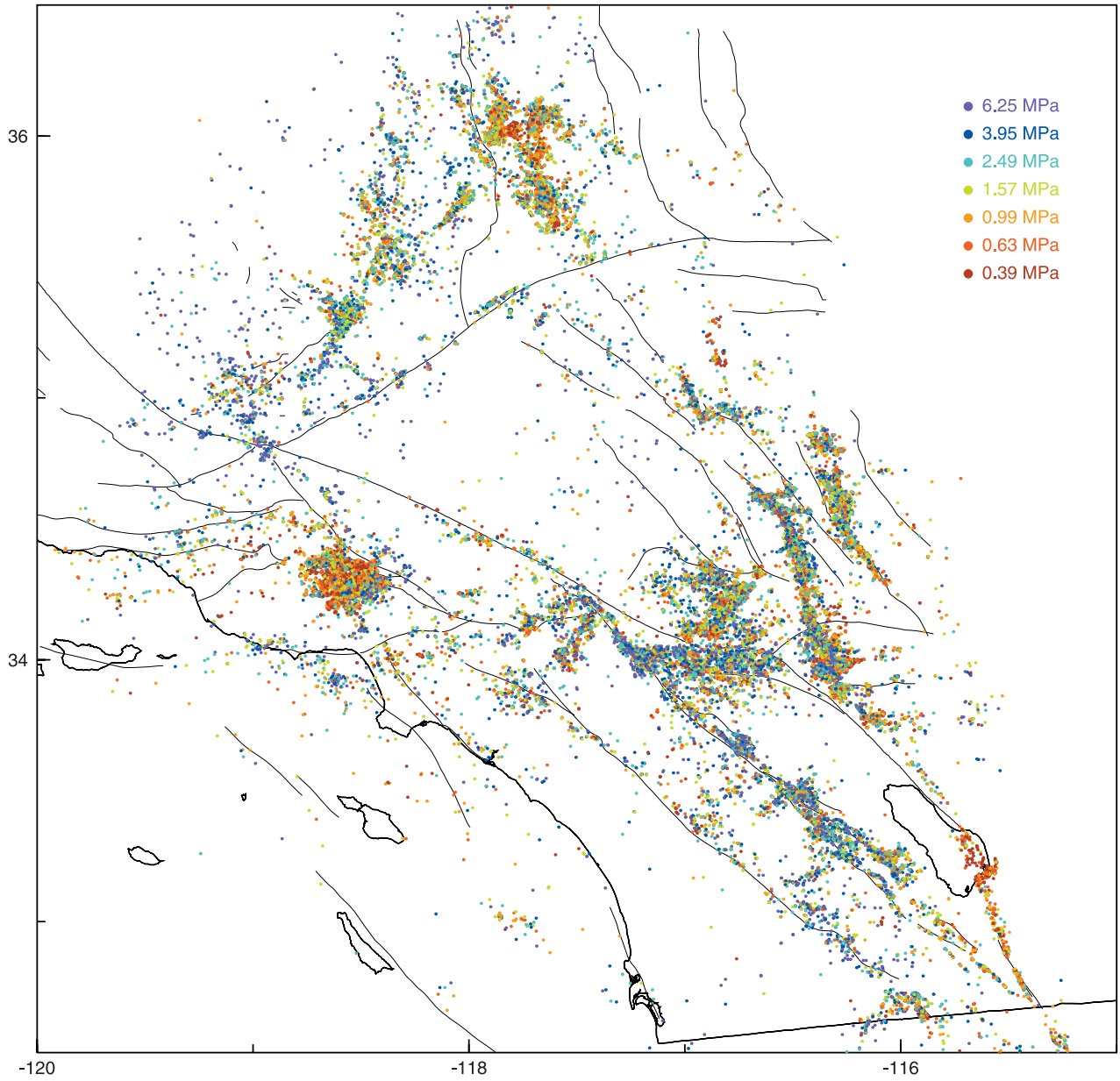

Figure 7. Individual stress drop estimates for 65,664 earthquakes, obtained using an inversion for source, receiver and traveltime dependent terms and a constant EGF method. Results are colored in equal increments of log $\Delta\sigma$.

that they would be hard to explain with reasonable differences in Q_α.

2.6. Multiple EGF Method

[49] To account for the possibility of near-source attenuation differences, we adapt the EGF method of section 2.5 to solve for a spatially varying EGF. The approach is similar to the source-specific station term (SSST) method used for earthquake location [*Richards-Dinger and Shearer*, 2000; *Lin and Shearer*, 2005; *Shearer et al.*, 2005]. For each target event, we identify the closest 500 neighboring events. We then average the 500 individual source spectra in moment bins and use the method described in section 2.3 to find the best fitting constant $\Delta\sigma$ model and an EGF specific to the 500 events. We subtract this EGF from the target log spectra and estimate the individual event $\Delta\sigma$ from the EGF-corrected spectrum. We compute a separate EGF for each earthquake; these EGFs will be similar but not necessarily identical for nearby events because the 500 neighboring events will vary for each target event.

[50] This method provides two $\Delta\sigma$ values for each event, an estimate for the event itself (Figure 8) and the best fitting constant $\Delta\sigma$ value for the 500 nearest events (Figure 9). A file containing these stress drop estimates can be obtained from http://igpphome.ucsd.edu/~shearer/Files/DELSIG/ or using anonymous ftp to ftp://mahi.ucsd.edu and going to the /pub/Shearer/DELSIG directory. A comparison between Figures 7 and 8 shows that implementing the spatially varying EGF method has a relatively small effect on the computed stress drops in most regions, compared to the

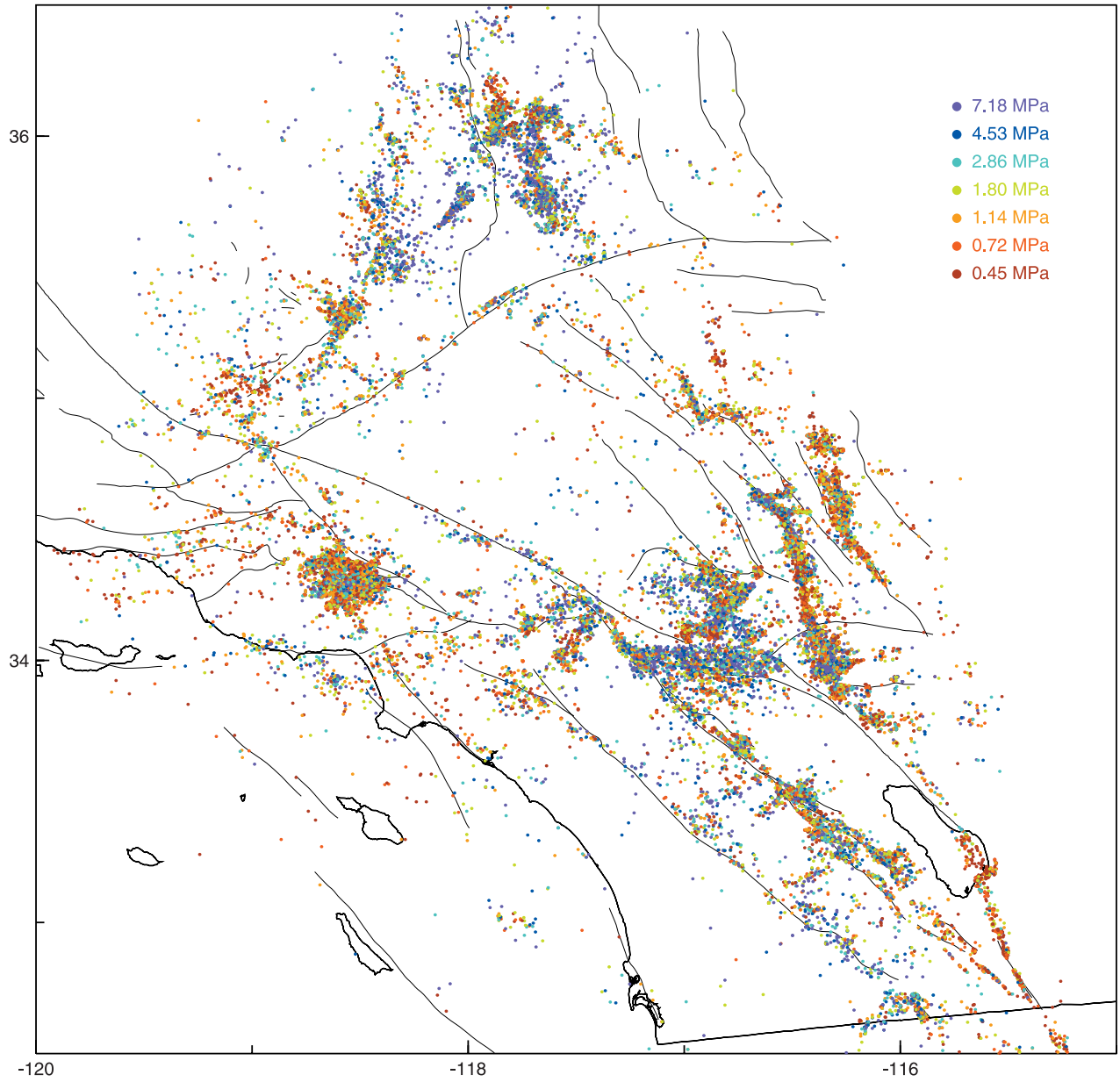

Figure 8. Individual stress drop estimates for 64,801 earthquakes, obtained using a source specific EGF method. Results are colored in equal increments of log $\Delta\sigma$. Results are quite similar to those obtained using the constant EGF approach (see Figure 7).

simpler approach of using a single EGF for the entire processed data set. The median stress drop is 1.80 MPa, close to the previous value of 1.57 MPa, and the patterns of high and low stress drop regions are largely unchanged, suggesting that the spatial variations in our observed earthquake spectra are dominated by differences in earthquake source properties rather than near-source Q variations. The most notable change between the single and multiple EGF results is in the Ridgecrest-Coso region (north of 35.5°N), where the stress drops increase significantly when the spatially varying EGF method is used. This probably is a result of relatively high attenuation in this area [e.g., *Young and Ward*, 1980; *Ho-Liu et al.*, 1988; *Wu and Lees*, 1996; *Hough et al.*, 1999; *Hauksson and Shearer*, 2005], which lowers the corner frequencies and inferred stress drops of events analyzed with the single EGF method (which implicitly assumes a laterally uniform Q model). Because in principle the multiple EGF method provides superior corrections for attenuation, we will focus on these results for the remainder of this paper.

[51] The individual event stress drop estimates span several orders of magnitude, as shown in Figure 10. At least some of this variation may be caused by random irregularities in individual spectra rather than true variations in source properties. Our most reliable measurements are obtained for those events that are recorded by the most stations because it is more likely that these random variations will be averaged out. Thus it is notable that stress drops exceeding 100 MPa are seen mainly for those events recorded on the fewest stations (see Figure 10). Anoma-

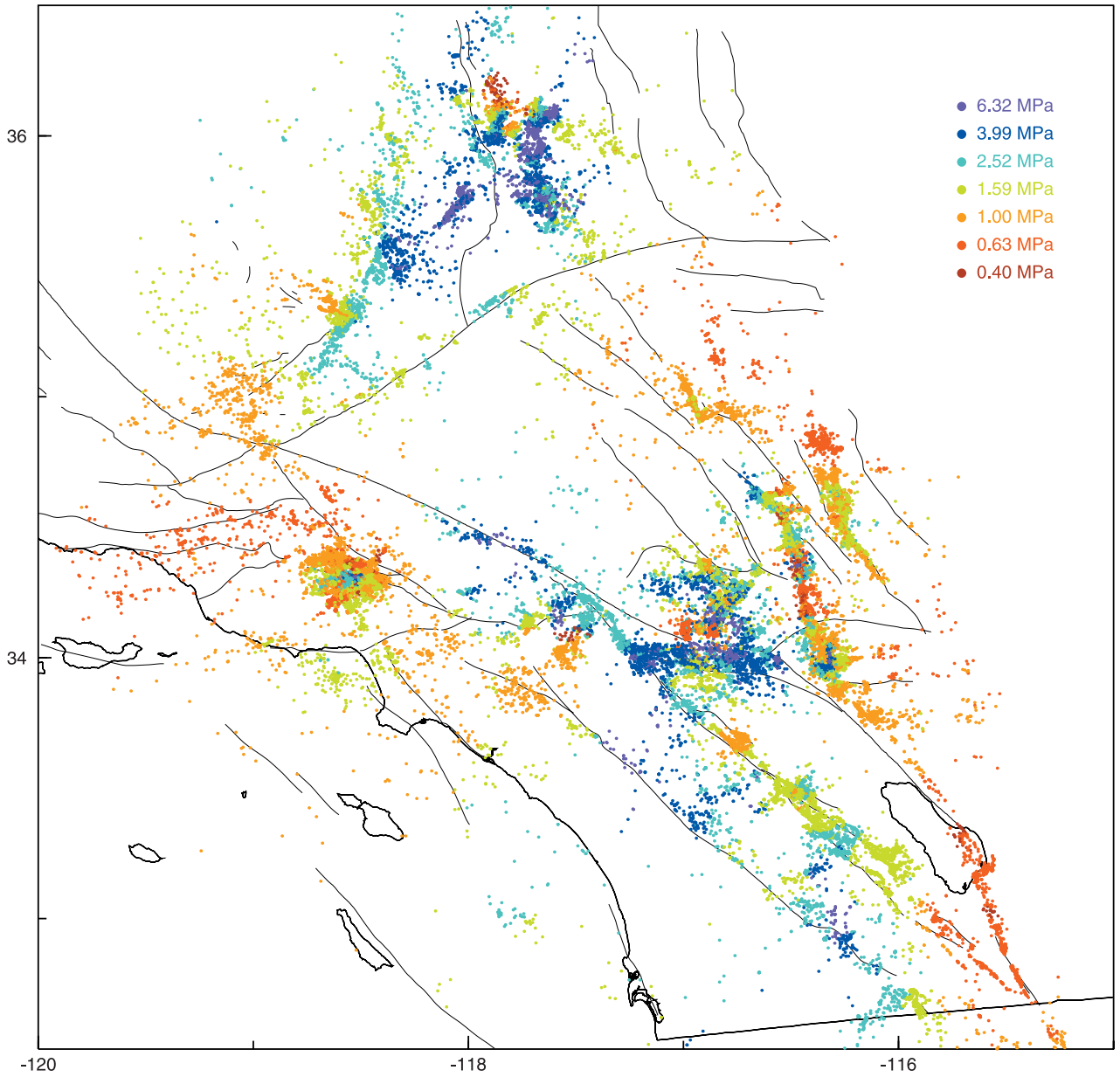

Figure 9. Results of fitting a constant stress drop model to each earthquake and its 500 nearest neighboring earthquakes. This represents a smoothed version of Figure 8 and provides a measure of average log stress drop. Results are colored in equal increments of log $\Delta\sigma$.

lously high stress drop events are difficult to reliably resolve because their corner frequencies may exceed the bandwidth of our data. Results for events recorded by at least 20 stations suggest that the true range of event stress drops is from about 0.2 to 20 MPa, with the bulk of the events between 0.5 and 8 MPa. This range generally agrees with results from other studies, including southern California [e.g., *Tucker and Brune*, 1973; *Thatcher and Hanks*, 1973; *Mori and Frankel*, 1990; *Abercrombie*, 1995; *Hough and Dreger*, 1995], Japan [e.g., *Jin et al.*, 2000] and Italy [e.g., *Bindi et al.*, 2001].

3. Comparisons to Other Parameters

[52] The 64,801 earthquake stress drop estimates plotted in Figure 8 are the main result of this study. Because of the large number of events, it should be possible to identify correlations between $\Delta\sigma$ and other parameters, even if the individual values of $\Delta\sigma$ exhibit significant scatter. In this section, we examine possible correlations between stress drop and other earthquake characteristics, such as moment, depth, focal mechanism and *b* value.

3.1. Moment Dependence of $\Delta\sigma$

[53] Figure 11 plots stress drop computed for individual events as a function of estimated moment magnitude. There is little, if any dependence of median $\Delta\sigma$ on moment, confirming our previous results obtained by fitting the stacked source spectra of Figure 5. There is some increased scatter into high $\Delta\sigma$ values for the smaller events where it may be hard to resolve corner frequencies above the 20 Hz limit of our modeling; as demonstrated in Figure 10, these

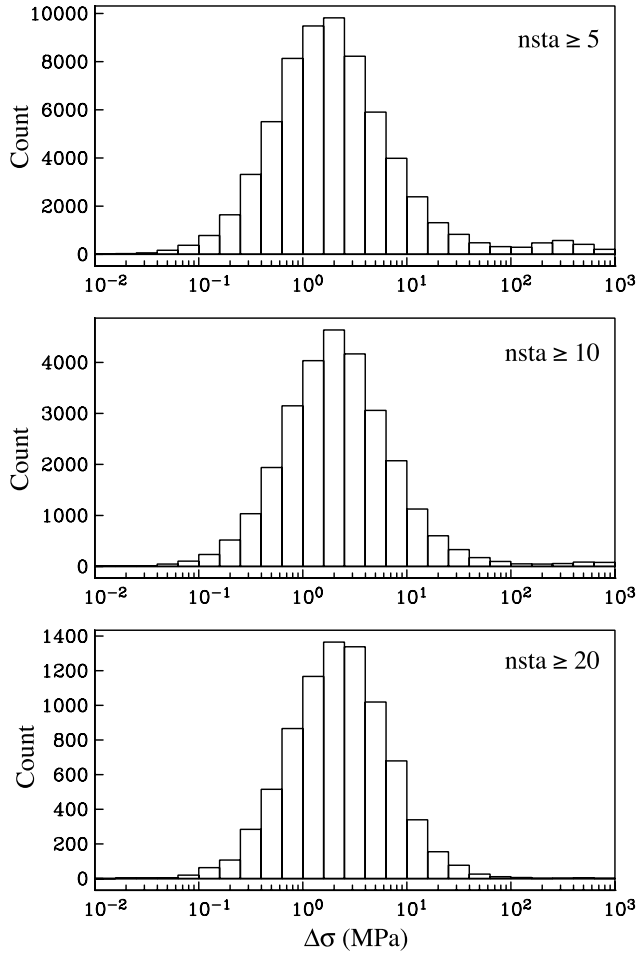

Figure 10. A histogram of the number of events as a function of estimated stress drop, for (top) earthquakes recorded by 5 or more stations, (middle) earthquakes recorded by 10 or more stations, and (bottom) earthquakes recorded by 20 or more stations. Note that the $\Delta\sigma > 100$ MPa estimates are only obtained for the most sparsely recorded events.

values are largely limited to events recorded by small numbers of stations. The question as to whether stress drop (or apparent stress) is constant or grows with moment has been a subject of continuing debate [e.g., *Kanamori et al.*, 1993; *Abercrombie*, 1995; *Choy and Boatwright*, 1995; *Mayeda and Walter*, 1996; *McGarr*, 1999; *Ide and Beroza*, 2001; *Izutani and Kanamori*, 2001; *Mori et al.*, 2003; *Ide et al.*, 2003; *Kanamori and Brodsky*, 2004; *Kanamori and Rivera*, 2004], which we cannot resolve given the limited magnitude range of our data set. For comparison, Figure 11 plots the slope of the $M_0^{1/4}$ scaling in apparent stress proposed by *Mayeda and Walter* [1996] over the magnitude range $3.3 \leq M \leq 7.3$. Our results do not follow this slope and suggest that M_W 2 to 3 events in southern California obey self-similar scaling.

[54] This supports self-similarity observations for comparable magnitude earthquakes in southern California by *Abercrombie* [1995] and *Prieto et al.* [2004]. Over a range extending to somewhat large earthquakes $M = 4$ to 5), *Mori and Frankel* [1990] found no correlation of $\Delta\sigma$ with moment for North Palm Springs aftershocks, and *Hough and Dreger* [1995] saw little scaling with moment for Joshua Tree aftershocks. However, *Hardebeck and Hauksson* [1997] found an increase in stress drop with moment for Northridge aftershocks and a number of studies have found some evidence for an increase in apparent stress with moment for southern California earthquakes, including *Kanamori et al.* [1993], *Abercrombie* [1995], *Mayeda and Walter* [1996] and *Mori et al.* [2003].

3.2. Depth Dependence of $\Delta\sigma$

[55] Figure 12 plots stress drop computed for individual events as a function of source depth. There is considerable scatter at all depths, but the median stress drop increases from 0.6 MPa near the surface to about 2.2 MPa at 8 km depth. Median stress drop is nearly constant between 8 km and 18 km depth and then drops off to about 1.3 MPa at 25 km depth. It is tempting to attribute the decrease in stress drop below 20 km to reduced fault strength because of increased temperatures [e.g., *Brace and Kohlstedt*, 1980; *Sibson*, 1984; *Tse and Rice*, 1986]. However, the decrease seen for the deepest earthquakes is dominated by the Northridge aftershocks, which have generally lower than average stress drops from 10 to 25 km depth. Because they make up a larger fraction of the earthquakes in our data set below 20 km than they do at other depths, their presence causes the decrease in median stress drop at large depths seen in Figure 11, which is not seen in other regions.

[56] However, the decrease in median stress drop estimates between 8 km and the surface is a robust feature of our results, and can be seen clearly in many different regions. At least some of this decrease can be explained

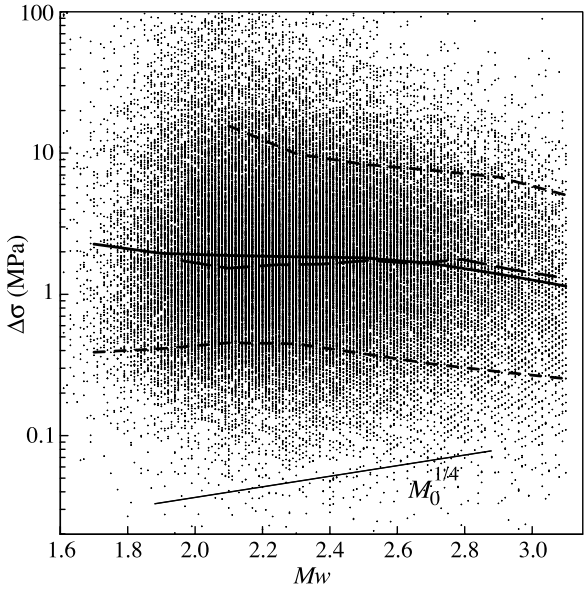

Figure 11. Individual earthquake stress drops versus estimated moment magnitude M_W. The solid line shows the median value in bins of 0.2 in M_W; the short dashed lines show the 10th and 90th percentiles. The long dashed line shows stress drop estimates obtained by fitting a variable $\Delta\sigma$ model to the spectra in Figure 5. The line at the bottom shows the predicted slope if stress drop is proportional to $M_0^{1/4}$.

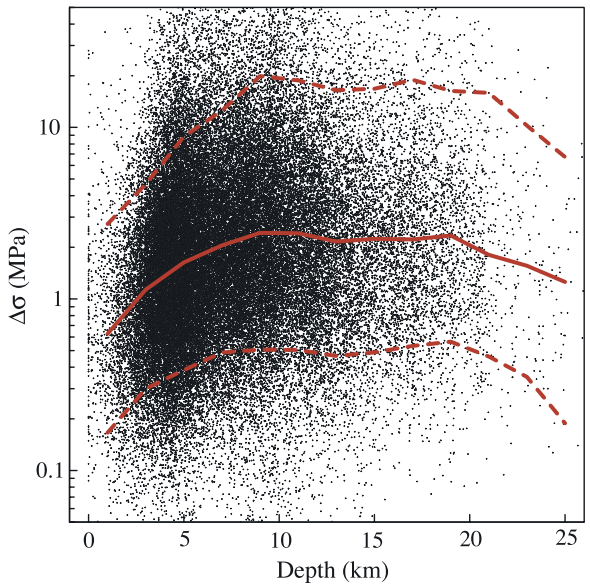

Figure 12. Individual earthquake stress drops versus depth. The solid line shows the median value in 2-km depth bins. The dashed lines show the 10th and 90th percentiles.

as a result of our assumption of a constant rupture velocity in equation (4). Because the shear velocity β decreases toward the surface, it is likely that rupture velocities are also reduced, which would imply that our stress drop estimates (based on a fixed rupture velocity) are biased toward smaller values. Indeed, a 35% reduction in shear velocity near the surface (and a constant rupture to shear velocity scaling) would be sufficient to explain our observations.

[57] Another possible source of bias is depth-dependent attenuation. Our first-order Q correction is sensitive only to the total source-to-receiver traveltime and does not take into account that some sources may be at shallow depths where attenuation is stronger than at greater depths. However, in principle the spatially varying EGF method should correct for attenuation differences caused by this effect. To test this further, we repeated the method of section 2.3 to fit for an EGF and constant stress drop model for stacks of the entire data set at different depth intervals, and found a similar increase in $\Delta\sigma$ with depth as seen in the median values of Figure 12. Our fundamental observation is that the source spectra of the shallower events become relatively depleted in high frequencies compared to the deeper events, even after correcting for Q and other path effects. This observation can be explained either in terms of lower stress drops or lower rupture velocities for the shallower events.

[58] Our observed variations in stress drop with depth are not as large as the lateral variations in median stress drop seen in Figures 8 and 9; these patterns remain even when depth corrections are applied to account for variations in average source depth among different regions. An increase in stress drop with event depth was previously noted by *Jones and Helmberger* [1996, 1998] in the eastern Transverse Ranges in California and by *Hardebeck and Hauksson* [2001] and *Mori et al.* [2003] for Northridge aftershocks. However, *Jin et al.* [2000] and *Kinoshita and Ohike* [2002] found little depth dependence in $\Delta\sigma$ along the Atotsugawa fault zone and near the Kanto region in Japan.

3.3. Focal Mechanism Dependence of $\Delta\sigma$

[59] Anderson faulting theory suggests that shear stress levels should be highest on reverse faults and least on normal faults [e.g., *Sibson*, 1974, 1982; *McGarr*, 1984; *Brune and Thatcher*, 2002]. To examine the possible dependence of our observed stress drops on the type of faulting, we use a new focal mechanism catalog for southern California (J. Hardebeck, personal communication, 2005) that was computed using both P polarity and S/P amplitude data [*Hardebeck and Shearer*, 2002, 2003]. Because of strict quality control criteria on the mechanism reliability, this catalog provides focal mechanisms for only about 6% of the over 60,000 events for which we have computed stress drops. We parameterize the focal mechanism type using the rakes, r1 and r2 (degrees), of the two nodal planes using the following algorithm (J. Hardebeck, personal communication, 2005):

```
if (abs(r1) >90) r1 = (180-abs(r1))*(r1/abs(r1))
if (abs(r2) >90) r2 = (180-abs(r2))*(r2/abs(r2))
if (abs(r1) < abs(r2)) then
r = r1
else
r = r2
end if
fptype = r/90
```

[60] The parameter fptype will vary from −1 (normal) to 0 (strike-slip) to 1 (reverse) and has the advantage of providing a single scalar value for characterizing the faulting type.

[61] Figure 13 (top) plots stress drop for 3895 earthquakes as a function of focal mechanism type. A great deal of scatter in $\Delta\sigma$ is seen for every type of fault geometry, but the median value of $\Delta\sigma$ decreases from 4 MPa for normal faults to 1.5 MPa for reverse faults. However, the decrease in $\Delta\sigma$ seen for reverse faults is dominated by the Northridge aftershocks, which tend to have lower than average stress drops. If these events are excluded (Figure 13, bottom), then there is no consistent difference in $\Delta\sigma$ between strike-slip and reverse faults, but a factor of $\sim$2 increase in median stress drop for normal faults remains. However, the normal fault earthquakes are not uniformly distributed across southern California; they are seen mainly in the southern Sierra/Ridgecrest-Coso region and the swath of seismicity near 34°N between Riverside and Desert Hot Springs (−117.2° to −116.2° longitude). These are both areas with higher than average stress drop estimates and the median stress drops of the normal faulting events are not significantly different from those of the other earthquakes in the same regions.

[62] Our results are contrary to expectations of Anderson theory, at least to the extent that stress drop is assumed proportional to shear stress, as well as several previous studies. *Cocco and Rovelli* [1989] found $\Delta\sigma$ was about 3 times bigger for thrust earthquakes compared to normal fault events for the Friuli sequence in Italy. *McGarr and Fletcher* [2002] found higher apparent stress for the reverse-faulting 1989 Loma Prieto and 1994 Northridge main shocks compared to the 1979 Imperial Valley, 1995 Kobe, and 1992 Landers main shocks.

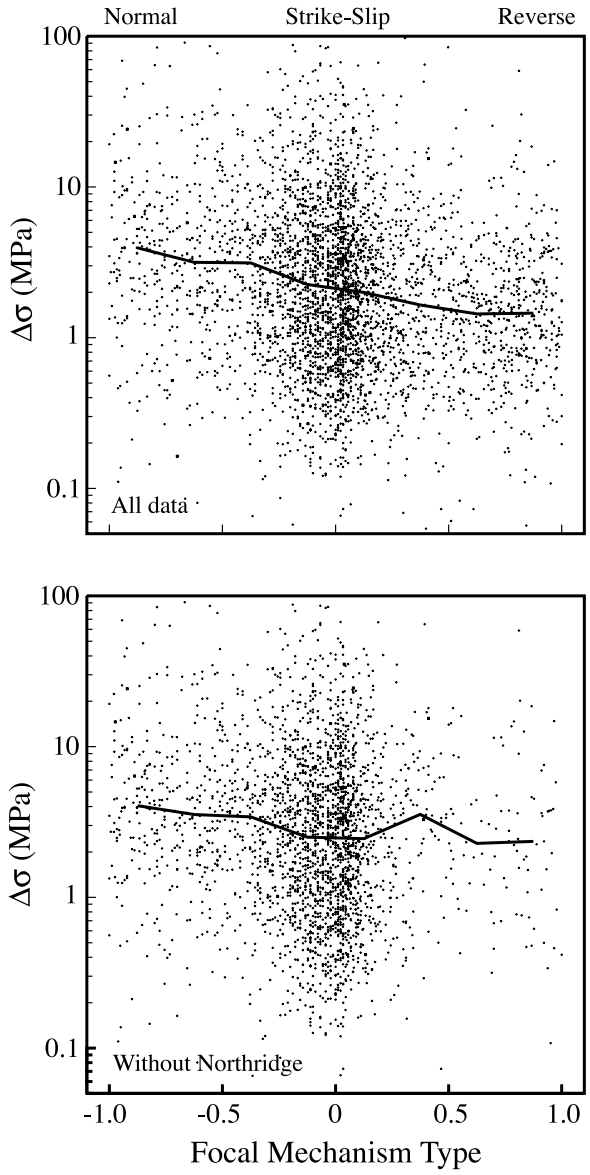

Figure 13. Individual earthquake stress drop estimates versus focal mechanism type (see text), for (top) the entire southern California data set and (bottom) excluding Northridge events.

3.4. The *b* Value Variations

[63] The increased number of small earthquakes compared to large earthquakes within a given volume is observed to fit a power law distribution:

$$\log N = a - bM \tag{5}$$

where N is the cumulative number of earthquakes of magnitude M or greater, a is a constant giving the overall productivity of the volume, and b (the "b value") gives the falloff rate in the number of large earthquakes compared to small earthquakes. Typically $b \sim 1$, indicating that there are 10 times fewer earthquakes for every unit increase in magnitude. However, spatial variations in b value exist and it has been hypothesized that b value is inversely correlated with shear stress [e.g., *Scholz*, 1968; *Wyss*, 1973; *Wiemer and Wyss*, 2002; *Amitrano*, 2003; *Schorlemmer et al.*, 2005].

[64] To test for a possible correlation between b value and our stress drop estimates in southern California, we map b value using the following method: (1) From the SHLK catalog [*Shearer et al.*, 2005], we extract 35,872 nighttime only events of $2 \leq M_L \leq 4$. We use nighttime events to eliminate quarry blasts and other artificial seismicity. (2) For each event, we identify the 500 nearest neighboring events. We then compute $N(M)$ and estimate the b value from a least squares fit to $\log(N)$, using only $N \neq 0$ points. This b value is then assigned to the target earthquake location. (3) The process is repeated for every target event to provide a b value estimate centered on every earthquake. The advantage of using a fixed number of earthquakes (e.g., 500) for this calculation, rather than a fixed radius or cell size, is that the resolution naturally adapts to the earthquake density.

[65] Figure 14 shows a map of the resulting b value distribution. There are many spatially coherent variations in b value, which ranges from about 0.7 to 1.6. However, a comparison to the smoothed stress drop values in Figure 9 shows that b value is not related in any simple way to our $\Delta\sigma$ estimates. Figure 15 plots b value (from Figure 14) versus $\Delta\sigma$ (from Figure 9) for common events between our b value and stress drop catalogs. There is no clear correlation, either positive or negative. There are many subtleties in computing b value [e.g., *Wiemer and Wyss*, 2002], and it is likely that different methods would yield different results than those shown in Figure 14. In addition, there are probably local regions in which either a positive or negative correlation can be observed. However, it seems unlikely that there exists a significant correlation across all of southern California between b value and $\Delta\sigma$. It is noteworthy that one of the clearest b value anomalies in southern California, the low b value of the Northridge aftershock sequence, is associated with lower than average $\Delta\sigma$ values. This is opposite to the inverse correlation proposed in many b value studies between b value and absolute stress.

4. Comparison to Other Studies

[66] Many previous studies have examined source spectra in southern California. Because of differences in modeling assumptions and the large scatter in estimated stress drops, direct comparisons of individual earthquakes are of limited value. However, some of the general features seen in our results (e.g., the range of $\Delta\sigma$ values, their depth dependence, and their regional variations) have been noted in several prior studies. Here we review previous work in southern California and identify consistencies and inconsistencies with our new results.

[67] *Wyss and Brune* [1971] examined short- to long-period amplitude ratios and estimated apparent stress for 227 M 3 to 6 earthquakes throughout California (from 1959 to 1968). Although their study measured apparent stress rather than stress drop, these parameters should be strongly correlated (see discussion in section 2.3). Their results indicated that the seismically active parts of major faults such as the San Andreas Fault (SAF) had lower than

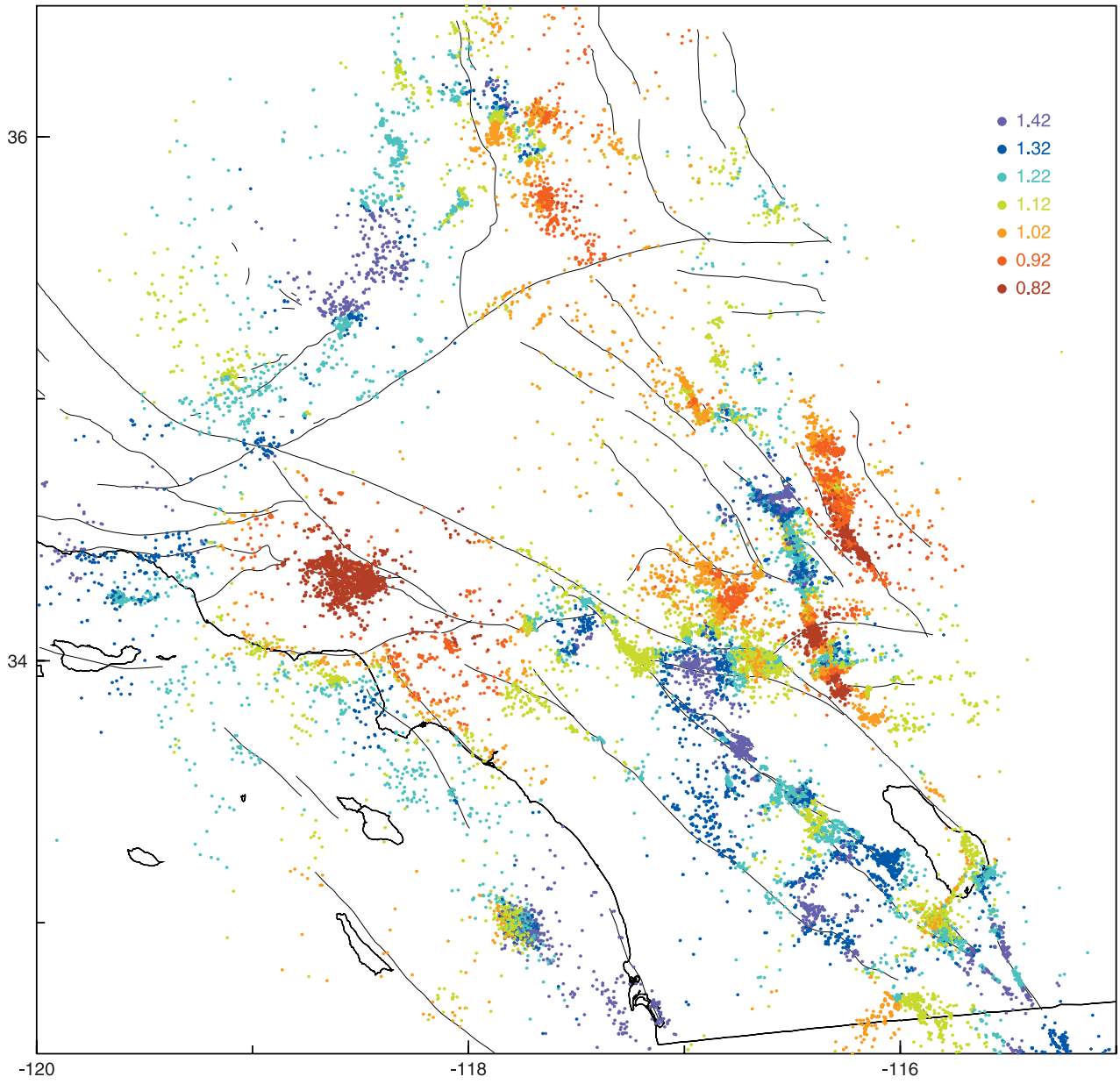

Figure 14. Estimated seismic *b* value for each earthquake and its 500 nearest neighbors, colored at 0.1 increments about the median value of 1.12. See text for details about the *b* value calculation.

average apparent stress, whereas the few earthquakes occurring on the seismically quiet portions of the SAF had somewhat higher apparent stress. This is consistent with our observations. The active faults in the Imperial Valley have low stress drops whereas the activity along the SAF between Palmdale and Wrightwood has higher than average stress drops. However, the general observation of Wyss and Brune that areas located off the main SAF fault system have relatively high apparent stress is not supported by our $\Delta\sigma$ estimates, which show no overall correlation with distance from the SAF (see Figure 9). Wyss and Brune noted high apparent stresses near San Bernardino and the north end of the San Jacinto fault; this agrees with our results, which indicate that this region has some of the highest average $\Delta\sigma$ values in southern California.

[68] Direct analysis of earthquake spectra expanded in the 1970s, following *Brune*'s [1970] classic paper on analysis of shear wave spectra and the increased availability of digital data. *Thatcher and Hanks* [1973] computed *S* wave spectra from 138 $M = 2$ to 7 earthquakes across southern California (from 1932 to 1971) and obtained $\Delta\sigma = 0.05$ to 20 MPa, an overall range that is very similar to our results. They noted a large scatter in $\Delta\sigma$ values even for nearby earthquakes and found little correlation between stress drop and magnitude or focal mechanism, in agreement with our analyses (with the exception of our higher observed stress drops for normal faults; it is not clear how many normal fault earthquakes they analyzed). Contrary to our findings, however, they also do not find a correlation with source depth, but this may be a result of the limited accuracy of the earthquake depths

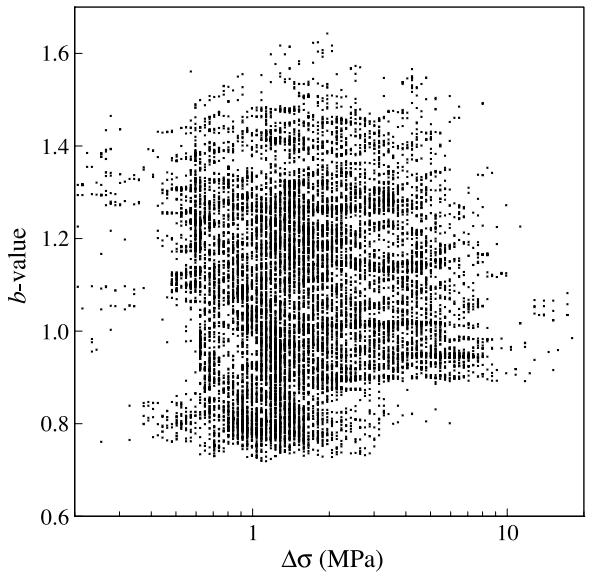

Figure 15. Estimated seismic *b* value versus stress drop for each earthquake and its 500 nearest neighbors.

used in their study. They found evidence for some regional variations in average stress, with the Imperial Valley events having lower than average $\Delta\sigma$ and Transverse Range and Kern County (aftershocks of the 1952 earthquake) events having relatively high stress drops. These differences are generally consistent with our results. *Tucker and Brune* [1973] computed *S* wave spectra for 167 M = 0.5 to 4.5 aftershocks of the 1971 San Fernando earthquake. They obtained $\Delta\sigma$ = 0.1 to 30 MPa, but argued that 10 MPa is a more likely upper limit owing to the effect of uncertainties on corner frequency estimates. They found a correlation between stress drop and moment, but in retrospect it seems likely that problems in the Q correction for the smaller events limit the significance of this correlation.

[69] In the 1980s, increased use of empirical Green's function (EGF) methods provided better Q corrections and improved spectral estimates for small earthquakes. A number of studies used data from the digital seismic network at Anza in southern California [*Berger et al.*, 1984]. *Frankel et al.* [1986] and *Frankel and Wennerberg* [1989] used an EGF approach to analyze *P* and *S* spectra from a small number of $M \sim 3$ Anza events and found $\Delta\sigma \sim 1$ to 6 MPa with no dependence on moment. These values were larger than most of the stress drops previously obtained for Anza events (without using EGF methods) by *Brune et al.* [1986] and *Fletcher et al.* [1987], who obtained $\Delta\sigma$ = 0.02 to 10 MPa for M = 0.7 to 3.8 earthquakes. These studies indicate a dependence of $\Delta\sigma$ on moment but it is possible that results for the smaller events are biased downward by Q effects. Recently, *Prieto et al.* [2004] used a stacking and EGF method to show constant scaling for a cluster of M 1.8 to 3.4 earthquakes at Anza.

[70] *Mori and Frankel* [1990] examined *P* spectra from 35 aftershocks (M = 3.4 to 4.4) of the 1986 North Palm Springs earthquake and used an EGF approach to obtain $\Delta\sigma$ = 0.3 to 8 MPa, with a tendency toward higher values near the edge of the fault plane. Our data do not start until 1989, but we observe generally higher than average stress drops for events in the same area. However, our results show considerable scatter in individual event stress drops across the region with no clear indication of lower stress drops near the hypocenter of the 1986 main shock.

[71] *Kanamori et al.* [1993] used data from the broadband TerraScope network to measure radiated seismic energy from *S* waves and estimate apparent stress and stress drop for 66 M 1.5 to 6 events. They obtained stress drop values between about 0.3 and 30 MPa. They found substantially higher stress drops for some main shocks compared to their aftershocks and noted generally higher stress drops for Transverse Range and Los Angeles Basin events. Our analysis is restricted to earthquakes of $M < 3.5$ so we cannot directly compare main shocks and aftershocks. We find generally higher average stress drops for Transverse Range events and earthquakes at the northern edge of the Los Angeles (LA) Basin but normal to below average $\Delta\sigma$ for the LA Basin itself.

[72] *Hough and Dreger* [1995] used an EGF method to analyze *P* and *S* spectra from 86 M 1.8 to 4.9 aftershocks of the 1992 Joshua Tree earthquake. They found large scatter in their stress drop estimates, which ranged from 0.1 to 100 MPa, with no resolvable dependence on moment. Many of the Hough and Dreger events are also included in our data set; a comparison shows a weak positive correlation in $\Delta\sigma$ values but with considerable scatter. In general, our results for Joshua tree aftershocks show $\Delta\sigma$ = 0.5 to 20 MPa, a smaller range than that found by Hough and Dreger.

[73] In an influential paper, *Abercrombie* [1995] studied *P* and *S* spectra for over 100 M_L −1 to 5.5 earthquakes recorded by a borehole seismometer at 2.5 km depth near Cajon Pass. Because attenuation effects are concentrated in the near surface, the borehole instrument can resolve corner frequencies for smaller events than is possible with surface stations. For her preferred attenuation model, she obtained $\Delta\sigma$ values ranging from about 0.2 to 50 MPa, with a median value near 3 MPa, and little, if any dependence upon moment. These results are in general agreement with our $\Delta\sigma$ values near Cajon Pass.

[74] *Jones and Helmberger* [1996] estimated stress drops from pulse width measurements obtained through synthetic seismogram modeling of $M > 3.9$ aftershocks of the 1992 Big Bear earthquake. They obtained relatively high stress drops (median $\Delta\sigma$ = 6.6 MPa) and a correlation with depth, with events deeper than 12 km having $\Delta\sigma > 10$ MPa. Although we cannot compare individual events, these results are in good agreement with our $\Delta\sigma$ maps, which have higher than average values for Big Bear aftershocks with a strong depth dependence. *Jones and Helmberger* [1998] used a similar approach to study 45 $M_W > 4$ aftershocks of the 1992 Joshua Tree and Landers earthquakes. They obtain log average stress drops of 3 MPa for the Joshua Tree aftershocks, 6.7 MPa for Landers events south of the Pinto Mountain fault, and 9.5 MPa for Landers events north of the Pinto Mountain fault. These values are somewhat higher than our median $\Delta\sigma$ results for the same faults. In addition, we observe significant along strike variations in $\Delta\sigma$ that are more complicated than simply a change in average value near the Pinto Mountain fault (see section 6).

[75] *Hardebeck and Hauksson* [1997] and *Mori et al.* [2003] estimated stress drops for aftershocks of the 1994

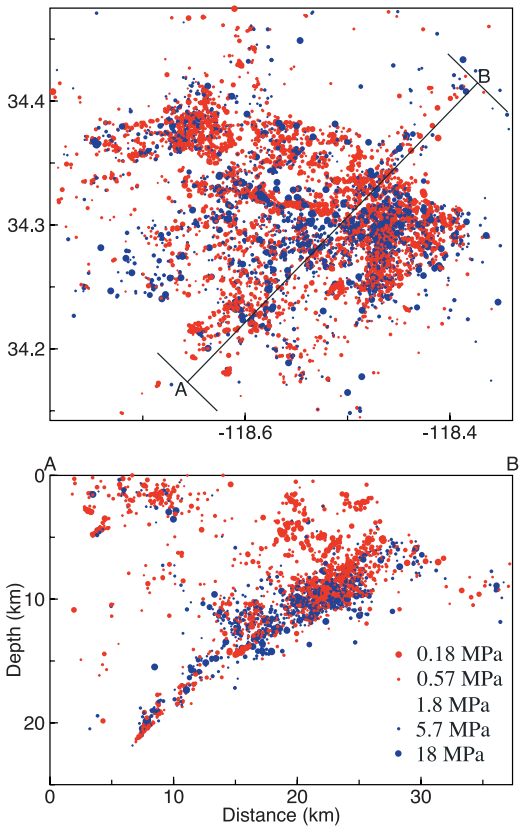

Figure 16. (top) Individual earthquake stress drop estimates for Northridge aftershocks. Deviations in log $\Delta\sigma$ about 1.8 MPa are scaled by circle size. Relatively low stress drops are plotted in red, relatively high stress drops are plotted in blue. (bottom) Cross section along the line AB in the map view.

Northridge earthquake. Hardebeck and Hauksson analyzed 279 M_L 2.5 to 4.0 aftershocks using a time domain approach on the P waves and obtained a log average value of $\Delta\sigma \sim$ 0.1 MPa. In contrast, Mori et al. obtained a median $\Delta\sigma$ of about 4 MPa using an EGF approach on P wave spectra for 47 $M \geq 4.0$ aftershocks. Both studies identified an apparent increase in average stress drop with depth. The large difference in these absolute stress drop estimates highlights the difficulty in direct comparisons between studies using different modeling assumptions. Our results for Northridge are plotted in Figure 16. We obtain a median stress drop of 1.2 MPa, intermediate between these prior studies but closer to the Mori et al. values. We also observe an increase in average stress drop with depth for Northridge, increasing from about 0.6 MPa near the surface to about 2.0 MPa at 15 km, with a slight drop off in average stress drop below 15 km.

5. Landers Aftershocks

[76] One notable feature of our stress drop estimates is strong along-strike variations in $\Delta\sigma$ seen in aftershocks of the 1992 Landers earthquake (see Figure 17). The Landers aftershocks have a slightly lower median stress drop than the southern California median, but this difference is small compared to the large variations among individual aftershocks. These variations are not random, but cluster into high and low stress drop regions. Because these changes in spectral properties occur over very short length scales, it is very unlikely that deficiencies in our attenuation corrections could be causing these patterns. They are almost certainly due to significant along-strike differences in source properties.

[77] Models of the Landers main shock rupture show considerable heterogeneity in slip along the fault. A key question is whether aftershock stress drops are related to differences in main shock slip. That is, one might expect stress to be reduced on patches of the fault with large slip and increased at the edges of these patches. To test this, we compare our $\Delta\sigma$ estimates with the Landers slip model of *Wald and Heaton* [1994], who used both geodetic and seismic data to invert for slip along three different profiles (see lines in Figure 17). Their preferred slip model (plotted in Figure 18) contains several patches of concentrated slip with up to 6 m of offset. Figure 18 also plots our stress drop results for individual aftershocks projected onto these cross sections.

[78] For the northern segment (Camp Rock/Emerson faults) a patch with high slip coincides with a cluster of low $\Delta\sigma$ aftershocks, which is bracketed by higher stress drop events. A weaker correlation between slip and low stress drop aftershocks is seen in the southern segment (Landers/Johnson Valley faults). Here the hypocenter location coincides with a low $\Delta\sigma$ aftershock region, but the modeled slip does not extend as deep as these aftershocks. There is a sharp transition between low and high $\Delta\sigma$ aftershocks at 9 to 12 km depth, just south of the hypocenter (at about 22 km distance in Figure 18), but this is about 5 km below the edge of the high-slip patch in the Wald and Heaton model. Further north in this fault segment there is a weak inverse correlation between slip and stress drop.

[79] This inverse correlation breaks down, however, in the middle fault segment (Homestead Valley fault), where a high slip patch coincides with higher than average $\Delta\sigma$ aftershocks. Thus the overall correlation for the entire model between slip and low stress drop aftershocks is fairly weak. However, it is not clear if all of the features in the Wald and Heaton slip model are reliably resolved. There are large differences among published Landers slip models (see model comparisons at http://www.seismo.ethz.ch/srcmod) and some do not include the large slip patch along the Homestead Valley segment. Given these uncertainties, it is difficult to rigorously test whether main shock slip and aftershock stress drops are inversely correlated, although Figure 18 suggests this may be true in several places. It would be interesting to perform hypothesis testing to see if slip models exist that satisfy the main shock geodetic and seismic data, while having their slip confined to the regions of low stress drop events.

6. Discussion

[80] These results, as well as those of many previous studies, show that earthquake stress drops, as measured by modeling their observed spectra, are extremely variable. Our $\Delta\sigma$ estimates across southern California range from about 0.2 to 20 MPa. These numbers could increase or

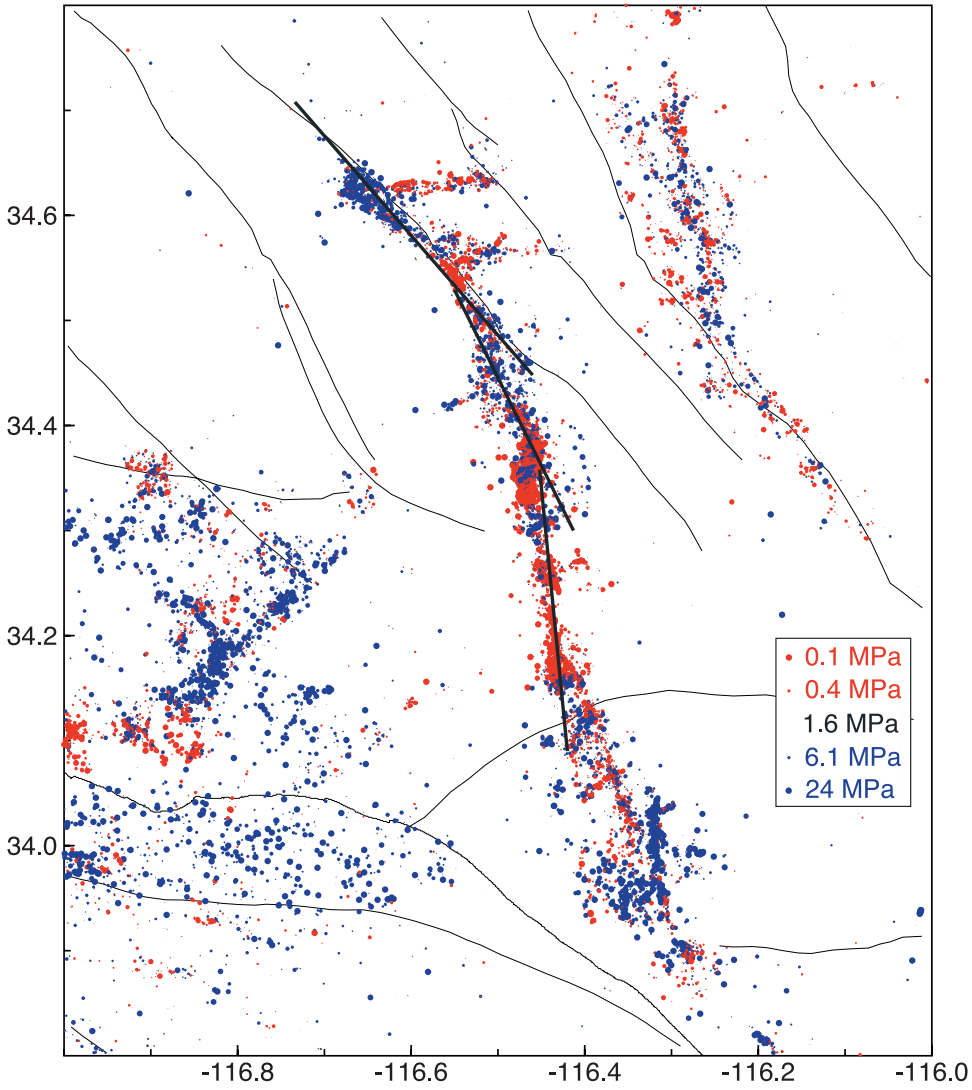

Figure 17. Individual earthquake stress drop estimates in the vicinity of the Joshua Tree, Landers, Big Bear, and Hector Mine aftershock sequences. Deviations in log $\Delta\sigma$ about 1.48 MPa are scaled by circle size. Relatively low stress drops are plotted in red, relatively high stress drops are plotted in blue. The three lines show the cross sections along the Landers fault that are plotted in Figure 18.

decrease depending upon certain modeling assumptions (e.g., assumed rupture velocity, etc.), but the variability in $\Delta\sigma$ over 2 orders of magnitude is a robust result. This spread may be partitioned into the regional variations in log average $\Delta\sigma$ plotted in Figure 9, which range from about 0.5 to 8 MPa, and a factor of $\sim$20 variation in $\Delta\sigma$ among nearby earthquakes. One consequence of this variability is that stress drop studies, even of compact source regions, need to examine large numbers of earthquakes to obtain statistically significant measures of stress drop differences. Our study is able to reliably resolve spatial variations in stress drop only by analyzing thousands of earthquakes.

[81] Our $\Delta\sigma$ estimates are derived from *P* wave corner frequency measurements using the approach of *Brune* [1970] as modified by *Madariaga* [1976]. The relationship between Brune-type stress drop estimates and static stress drops has been debated [e.g., *Andrews*, 1986; *Snoke*, 1987; *Hough*, 1996]. However, for large earthquakes, static stress drop can be measured more directly from observed surface deformation, and geodetic studies are generally consistent with seismic studies in showing that $\Delta\sigma$ varies from about 0.2 to 20 MPa. Exploring the theoretical validity of various models for computing earthquake stress parameters from observed spectra is beyond the scope of this paper. Therefore we wish to emphasize that our most important result is in documenting the large differences in the shapes of earthquake source spectra across southern California, even after corrections are applied to remove attenuation and other path effects. These differences are real and reflect significant amplitude variations in high-frequency *P* waves radiated from the source among earthquakes of equal moment, regardless of the details of how these differences are translated into stress drop or apparent stress estimates. Differences in modeling assumptions could easily change our stress estimates by factors of two or more. However, because we compute $\Delta\sigma$ in a consistent way for the over

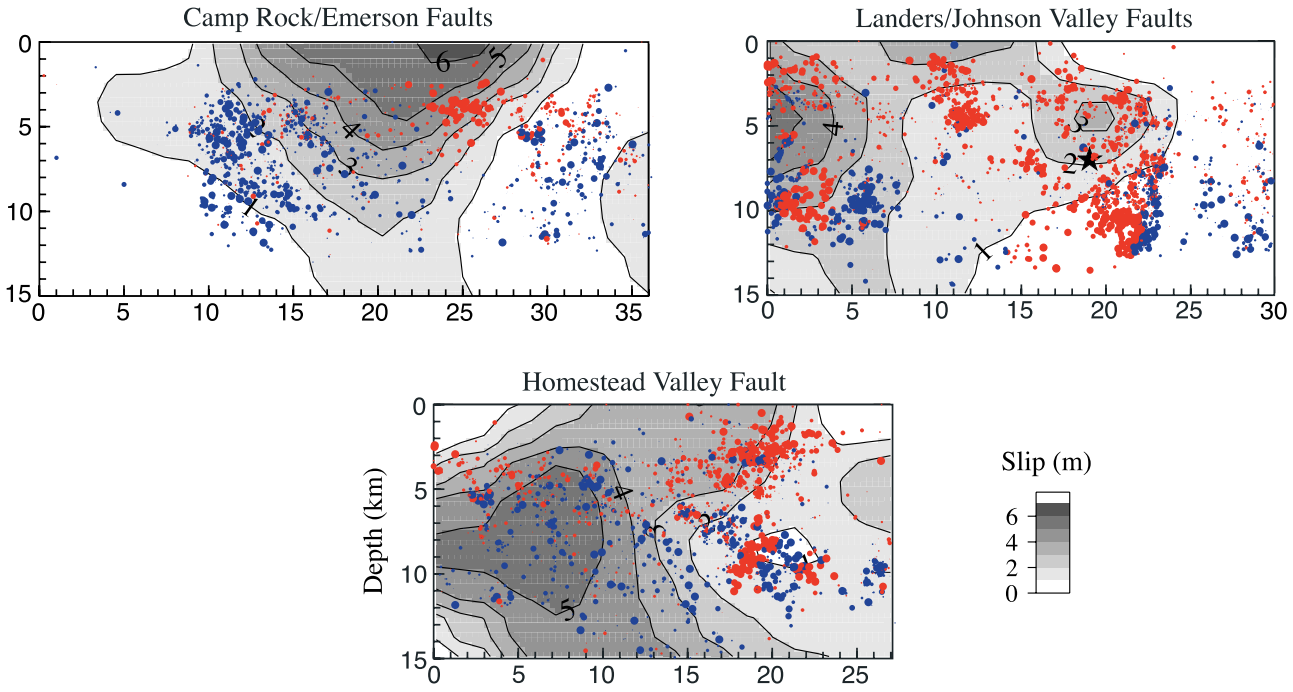

Figure 18. Cross section of Landers aftershock stress drop estimates compared to the main shock slip model of *Wald and Heaton* [1994]. Deviations in log $\Delta\sigma$ about 1.48 MPa are scaled by circle size. Relatively low stress drops are plotted in red; relatively high stress drops are plotted in blue. The gray scale contours show slip in meters for the Wald and Heaton model.

60,000 earthquakes in our study, the relative sizes of $\Delta\sigma$ provide a reliable measure of the differences among events.

[82] Our stress drop estimates for individual earthquakes across southern California do not correlate with moment, seismic *b* value, or distance from major faults. However, a significant correlation exists between $\Delta\sigma$ and depth in the upper crust, with median $\Delta\sigma$ increasing from 0.6 MPa near the surface to 2.2 MPa at 8 km depth. We observe a higher median stress drop for normal faulting earthquakes across southern California, compared to strike-slip and reverse faulting events, but this difference is not seen among events within the same region. Northridge aftershocks, which include many reverse faulting events, have lower than average stress drops compared to the rest of southern California. There is a suggestion that stress drop variations among Landers aftershocks may be inversely correlated with main shock slip, but this is far from a conclusive association. So far we have not been able to resolve any temporal variations in average stress drop, but our ability to detect such variations is limited by the 13 year span of our data, the large scatter in individual $\Delta\sigma$ estimates, and the general nonstationarity of seismicity patterns.

[83] Interpretation of the stress drop variations plotted in Figure 9 in terms of southern California tectonics is complicated by the unknown relationship between stress drop and absolute stress. Seismic wave observations do not directly constrain absolute stress levels. Measuring absolute shear stress at depth is a difficult problem that touches on many controversial subjects such as the strength of faults and the heat flow paradox. One view [e.g., *Scholz*, 2000] is that average crustal shear stress levels ($\overline{\sigma}$) are much higher than earthquake stress drops, consistent with laboratory results for rock friction. This may be termed the strong fault model, in which case earthquake stress drops release only a small fraction of the initial stress. An opposing view [e.g., *Zoback et al.*, 1987; *Brune and Thatcher*, 2002] is that at least some faults are much weaker than predicted by rock sliding experiments and that earthquake stress drops are a significant fraction of the background stress. This predicts that less total energy is released by earthquakes than in the strong fault model.

[84] Absolute stress estimates consistent with the strong fault model can be estimated from Andersonian faulting theory, which predicts an increase in $\overline{\sigma}$ with depth with values at 10 km depth ranging from 50 to 80 MPa for normal faults, 80 to 130 MPa for strike slip faults, and 200 to 320 MPa for reverse faults [*Brune and Thatcher*, 2002; see also *Sibson*, 1984]. We observe an increase in $\Delta\sigma$ with depth but only to about 8 km. In addition, we observe a large variation in $\Delta\sigma$ among different earthquakes at the same depth and an increase rather than a decrease in stress drop for regions containing normal fault earthquakes. Thus, if the strong fault model is correct, the observed stress drop variations are most likely dominated by variations in scaling between $\Delta\sigma$ and $\overline{\sigma}$.

[85] For the weak fault model, $\overline{\sigma} \leq 20$ MPa [e.g., *Brune and Thatcher*, 2002]. If the average $\Delta\sigma/\overline{\sigma}$ ratio does not vary spatially across southern California, then our observations of no noticeable drop in $\Delta\sigma$ near the SAF argue against the SAF being weak compared to other crustal faults in southern California. In general, there is no clear correlation between observed stress drop and distance from major faults in southern California; thus differences noted between interplate and intraplate stress drops [e.g., *Kanamori and*

Anderson, 1975; Scholz, 1986; *Zhuo and Kanamori*, 1987] do not appear to apply locally within southern California. A possible exception to this observation is the relatively low stress drops for Imperial Valley earthquakes. In this case, the faults may have reduced strength at depth owing to higher heat flow but the mechanism by which this would cause low stress drop earthquakes in the brittle crust is not clear.

[86] It is tempting to ascribe the high stress drops observed for the eastern Transverse ranges and at the north end of the San Jacinto fault to the effects of compression near the Big Bend in the SAF. However, there are almost no reverse fault mechanisms among these high $\Delta\sigma$ clusters of events, which are dominated by normal and strike-slip faulting. In general, there does not appear to be a simple explanation for the complex spatial variations in average $\Delta\sigma$ that we observe, nor a straightforward way to estimate absolute stress from our results. A possible avenue toward constraining the scaling between stress drop and absolute stress would be to examine possible temporal variations in stress drop as a result of a change in static stress imposed by a large earthquake. This approach would be similar to the focal mechanism analyses of *Hauksson* [1994] and *Hardebeck and Hauksson* [2001], who found some evidence for stress rotation in response to main shock stress changes [an interpretation disputed by *Townend and Zoback*, 2001]. We have not found a clear case of a temporal change in average $\Delta\sigma$ near a large earthquake, but our results are limited by the lack of premain shock seismicity in the vicinity of most large earthquakes during our study period. Further study of the relationship between main shock slip and aftershock stress drops is warranted. If the suggested inverse correlation between fault slip and aftershock stress drops for the 1992 Landers earthquake can be confirmed, this would provide constraints on the relationship between stress drop and absolute stress variations, given that the amount of main shock stress drop can be computed for a given slip model.

7. Conclusions

[87] Our method provides an efficient and self-consistent way to analyze spectra from large waveform archives, such as those now available from many seismic networks. We introduce a new way to compute empirical Green's functions (EGF) for distributed seismicity that provides results for the smaller earthquakes. Our results are generally consistent with prior studies, but we examine a much larger number of earthquakes. We show that substantial variations in earthquake source spectral properties for $M_W = 2$ to 3 earthquakes exist in southern California, including spatially coherent patterns in average stress drop, which do not appear to correlate in any simple way to tectonic features, moment, or *b* value. The clearest correlations are an increase in stress drop (or an increase in rupture velocity) with depth within the top 8 km of the crust and a higher median stress drop in regions containing significant numbers of normal fault earthquakes. Significant along-strike variations in stress drop are observed for aftershocks of the 1992 Landers earthquake; there is a suggestion that low stress drop aftershocks may correlate with high-slip patches during the main shock rupture.

[88] **Acknowledgments.** We thank the personnel of the USGS/Caltech Southern California Seismic Network who pick and archive the seismograms and the Southern California Earthquake Center (SCEC) for distributing the data; we especially thank Vikki Appel, who facilitated access to the database. We thank Susan Hough and Gregory Beroza for constructive reviews. Funding for this research was provided by NEHRP/USGS grant 03HQPA0001. This research was also supported by the Southern California Earthquake Center, which is funded by NSF Cooperative Agreement EAR-0106924 and USGS Cooperative Agreement 02HQAG0008. This is SCEC contribution 919 and contribution 9121 of Division of Geological and Planetary Sciences, California Institute of Technology, Pasadena.

References

Abercrombie, R. E. (1995), Earthquake source scaling relationships from −1 to 5 M_L using seismogram recorded at 2.5-km depth, *J. Geophys. Res.*, *100*, 24,015–24,036.

Abercrombie, R. E. (1996), The magnitude-frequency distribution of earthquakes recorded with deep seismometers at Cajon Pass, southern California, *Tectonophysics*, *261*, 1–7.

Aki, K. (1967), Scaling law of seismic spectrum, *J. Geophys. Res.*, *72*, 1217–1231.

Amitrano, D. (2003), Brittle-ductile transition and associated seismicity: Experimental and numerical studies and relationship with the b value, *J. Geophys. Res.*, *108*(B1), 2044, doi:10.1029/2001JB000680.

Andrews, D. J. (1986), Objective determination of source parameters and similarity of earthquakes of different size, in *Earthquake Source Mechanics*, *Geophys. Monogr. Ser.*, vol. 37, edited by S. Das, J. Boatwright, and C. H. Scholz, pp. 259–267, AGU, Washington, D. C.

Bakun, W. H. (1984), Seismic moments, local magnitudes, and coda-duration magnitudes for earthquakes in central California, *Bull. Seismol. Soc. Am.*, *74*, 439–458.

Beeler, N. M., T.-F. Wong, and S. H. Hickman (2003), On the expected relationships among apparent stress, static stress drop, effective shear fracture energy, and efficiency, *Bull. Seismol. Soc. Am.*, *93*, 1381–1389.

Ben-Zion, Y., and L. Zhu (2002), Potency-magnitude scaling relations for southern California earthquakes with $1.0 < M_L < 7.0$, *Geophys. J. Int.*, *148*, F1–F5.

Berger, J., L. Baker, J. Brune, J. Fletcher, T. Hanks, and F. Vernon (1984), The Anza array: A high-dynamic-range, broadband, digitally radiometered seismic array, *Bull. Seismol. Soc. Am.*, *74*, 1469–1481.

Bindi, D., D. Spallarossa, P. Augliera, and M. Cattaneo (2001), Source parameters estimated from the aftershocks of the 1997 Umbria-Marche (Italy) seismic sequence, *Bull. Seismol. Soc. Am.*, *91*, 448–455.

Boatwright, J., J. B. Fletcher, and T. E. Fumal (1991), A general inversion scheme for source, site, and propagation characteristics using multiply recorded sets of moderate-sized earthquakes, *Bull. Seismol. Soc. Am.*, *81*, 1754–1782.

Brace, W. F., and D. L. Kohlstedt (1980), Limits on lithospheric stress imposed by laboratory experiments, *J. Geophys. Res.*, *85*, 6248–6252.

Brune, J. N. (1970), Tectonic stress and spectra of seismic shear waves from earthquakes, *J. Geophys. Res.*, *75*, 4997–5009.

Brune, J. N., and W. Thatcher (2002), Strength and energetics of active fault zones, in *International Handbook of Earthquake and Engineering Seismology*, vol. 81A, pp. 569–588, Int. Assoc. of Seismol. and Phys. of the Earth's Inter., Trieste, Italy.

Brune, J. N., R. J. Archuleta, and S. Hartzell (1979), Far-field S-wave spectra, corner frequencies, and pulse shapes, *J. Geophys. Res.*, *84*, 2262–2272.

Brune, J. N., J. Fletcher, F. Vernon, L. Haar, T. Hanks, and J. Berger (1986), Low stress-drop earthquakes in the light of new data from the Anza, California telemetered digital array, in *Earthquake Source Mechanics*, *Geophys. Monogr. Ser.*, vol. 37, pp. 237–206, AGU, Washington, D. C.

Choy, G. L., and J. L. Boatwright (1995), Global patterns of radiated seismic energy and apparent stress, *J. Geophys. Res.*, *100*, 18,205–18,228.

Cocco, M., and A. Rovelli (1989), Evidence for the variation of stress drop between normal and thrust faulting earthquakes in Italy, *J. Geophys. Res.*, *94*, 9399–9416.

Di Bona, M., and A. Rovelli (1988), Effects of the bandwidth limitation on stress drops estimated from integrals of the ground motion, *Bull. Seismol. Soc. Am.*, *78*, 1818–1825.

Fletcher, J., L. Haar, T. Hanks, L. Baker, F. Vernon, J. Berger, and J. Brune (1987), The digital array at Anza, California: Processing and initial interpretation of source parameters, *J. Geophys. Res.*, *92*, 369–382.

Frankel, A., and L. Wennerberg (1989), Microearthquake spectra from the Anza, California, seismic network: Site response and source scaling, *Bull. Seismol. Soc. Am.*, *79*, 581–609.

Frankel, A., J. Fletcher, F. Vernon, L. Haar, J. Berger, T. Hanks, and J. Brune (1986), Rupture characteristics and tomographic source imaging of $M_L \sim 3$ earthquakes near Anza, southern California, *J. Geophys. Res.*, *91*, 12,633–12,650.

Hanks, T. C., and D. M. Boore (1984), Moment-magnitude relations in theory and practice, *J. Geophys. Res.*, *89*, 6229–6235.

Hardebeck, J. L., and E. Hauksson (1997), Static stress drop in the 1994 Northridge, California, aftershock sequence, *Bull. Seismol. Soc. Am.*, *87*, 1495–1501.

Hardebeck, J. L., and E. Hauksson (2001), Crustal stress field in southern California and its implications for fault mechanics, *J. Geophys. Res.*, *106*, 21,859–21,882.

Hardebeck, J. L., and P. M. Shearer (2002), A new method for determining first-motion focal mechanisms, *Bull. Seismol. Soc. Am.*, *92*, 2264–2276.

Hardebeck, J. L., and P. M. Shearer (2003), Using S/P amplitude ratios to constrain the focal mechanisms of small earthquakes, *Bull. Seismol. Soc. Am.*, *93*, 2434–2444.

Hauksson, E. (1994), State of stress from focal mechanisms before and after the 1992 Landers earthquake sequence, *Bull. Seismol. Soc. Am.*, *84*, 917–934.

Hauksson, E., and P. Shearer (2005), Southern California hypocenter relocation with waveform cross-correlation: Part 1. Results using the double-difference method, *Bull. Seismol. Soc. Am.*, *95*, 896–903.

Hauksson, E., and P. M. Shearer (2006), Attenuation models (Q_P and Q_S) in three dimensions of the southern California crust: Inferred fluid saturation at seismogenic depths, *J. Geophys. Res.*, *111*, B05302, doi:10.1029/2005JB003947.

Ho-Liu, P., H. Kanamori, and R. W. Clayton (1988), Applications of attenuation tomography to Imperial Valley and Coso-Indian Wells region, southern California, *J. Geophys. Res.*, *93*, 10,501–10,520.

Hough, S. E. (1996), Observational constraints on earthquake source scaling: Understanding the limits in resolution, *Tectonophysics*, *261*, 83–95.

Hough, S. E. (1997), Empirical Green's function analysis: Taking the next step, *J. Geophys. Res.*, *102*, 5369–5384.

Hough, S. E., and D. S. Dreger (1995), Source parameters of the 23 April 1992 M 6.1 Joshua Tree, California, earthquake and its aftershocks: Empirical Green's function analysis of GEOS and TERRAscope data, *Bull. Seismol. Soc. Am.*, *85*, 1576–1590.

Hough, S. E., J. M. Lees, and F. Monastero (1999), Attenuation and source properties at the Coso Geothermal area, California, *Bull. Seismol. Soc. Am.*, *89*, 1606–1619.

Humphrey, J. R., and J. G. Anderson (1994), Seismic source parameters from the Guerrero subduction zone, *Bull. Seismol. Soc. Am.*, *84*, 1754–1769.

Ide, S., and G. C. Beroza (2001), Does apparent stress vary with earthquake size?, *Geophys. Res. Lett.*, *28*, 3349–3352.

Ide, S., G. C. Beroza, S. G. Prejean, and W. L. Ellsworth (2003), Apparent break in earthquake scaling due to path and site effects on deep borehole recordings, *J. Geophys. Res.*, *108*(B5), 2271, doi:10.1029/2001JB001617.

Izutani, Y., and H. Kanamori (2001), Scale-dependance of seismic energy-to-moment ratio for strike–slip earthquakes in Japan, *Geophys. Res. Lett.*, *28*, 4007–4010.

Jin, A., C. A. Moya, and M. Ando (2000), Simultaneous determination of site responses and source parameters of small earthquakes along the Atotsugawa fault zone, central Japan, *Bull. Seismol. Soc. Am.*, *90*, 1430–1445.

Jones, L. E., and D. V. Helmberger (1996), Seismicity and stress-drop in the eastern Transverse ranges, southern California, *Geophys. Res. Lett.*, *23*, 233–236.

Jones, L. E., and D. V. Helmberger (1998), Earthquake source parameters and fault kinematics in the Eastern California Shear Zone, *J. Geophys. Res.*, *88*, 1337–1352.

Kanamori, H. (1977), The energy release in great earthquakes, *J. Geophys. Res.*, *82*, 2981–2987.

Kanamori, H., and D. Anderson (1975), Theoretical basis for some empirical laws of seismology, *Bull. Seismol. Soc. Am.*, *65*, 1073–1095.

Kanamori, H., and E. E. Brodsky (2004), The physics of earthquakes, *Rep. Prog. Phys.*, *67*, 1429–1496.

Kanamori, H., and L. Rivera (2004), Static and dynamic scaling relations for earthquakes and their implications for rupture speed and stress drop, *Bull. Seismol. Soc. Am.*, *94*, 314–319.

Kanamori, H., J. Mori, E. Hauksson, T. H. Heaton, L. K. Hutton, and L. Jones (1993), Determination of earthquake energy release and M_L using TERRAscope, *Bull. Seismol. Soc. Am.*, *83*, 330–346.

Kinoshita, S., and M. Ohike (2002), Scaling relations of earthquakes that occurred in the upper part of the Philippine Sea plate beneath the Kanto region, Japan, estimated by means of borehole recordings, *Bull. Seismol. Soc. Am.*, *92*, 611–624.

Lin, G., and P. Shearer (2005), Tests of relative earthquake location techniques using synthetic data, *J. Geophys. Res.*, *110*, B04304, doi:10.1029/2004JB003380.

Madariaga, R. (1976), Dynamics of an expanding circular fault, *Bull. Seismol. Soc. Am.*, *66*, 639–666.

Mayeda, K., and W. R. Walter (1996), Moment, energy, stress drop, and source spectra of western United States earthquakes from regional coda envelopes, *J. Geophys. Res.*, *101*, 11,195–11,208.

McGarr, A. (1984), Scaling of ground motion parameters, state of stress, and focal depth, *J. Geophys. Res.*, *89*, 6969–6979.

McGarr, A. (1999), On relating apparent stress to the stress causing earthquake fault slip, *J. Geophys. Res.*, *104*, 3001–3003.

McGarr, A., and J. B. Fletcher (2002), Mapping apparent stress and energy radiation over fault zones of major earthquakes, *Bull. Seismol. Soc. Am.*, *92*, 1633–1646.

Mori, J., and A. Frankel (1990), Source parameters for small events associated with the 1986 North Palm Springs, California, earthquake determined using empirical Green functions, *Bull. Seismol. Soc. Am.*, *80*, 278–295.

Mori, J., R. E. Abercrombie, and H. Kanamori (2003), Stress drops and radiated energies of aftershocks of the 1994 Northridge, California, earthquake, *J. Geophys. Res.*, *108*(B11), 2545, doi:10.1029/2001JB000474.

Mueller, C. S. (1985), Source pulse enhancement by deconvolution of an empirical Green's function, *Geophys. Res. Lett.*, *12*, 33–36.

Park, J., C. R. Lindberg, and F. L. Vernon (1987), Multitaper spectral analysis of high frequency seismograms, *J. Geophys. Res.*, *92*, 12,675–12,648.

Prieto, G. A., P. M. Shearer, F. L. Vernon, and D. Kilb (2004), Earthquake source scaling and self-similarity estimation from stacking P and S spectra, *J. Geophys. Res.*, *109*, B08310, doi:10.1029/2004JB003084.

Richards-Dinger, K. B., and P. M. Shearer (2000), Earthquake locations in southern California obtained using source-specific station terms, *J. Geophys Res.*, *105*, 10,939–10,960.

Savage, J. C., and M. D. Wood (1971), The relation between apparent stress and stress drop, *Bull. Seismol. Soc. Am.*, *61*, 1381–1388.

Schlotterbeck, B. A., and G. A. Abers (2001), Three-dimensional attenuation variations in southern California, *J. Geophys. Res.*, *106*, 30,719–30,735.

Scholz, C. H. (1968), The frequency-magnitude relation of microfracturing in rock and its relation to earthquakes, *Bull. Seismol. Soc. Am.*, *58*, 399–415.

Scholz, C. H. (2000), Evidence for a strong San Andreas fault, *Geology*, *28*, 163–166.

Scholz, C. H., C. A. Aviles, and S. G. Wesnousky (1986), Scaling differences between large interplate and intraplate earthquakes, *Bull. Seismol. Soc. Am.*, *76*, 65–70.

Schorlemmer, D., S. Wiemer, and M. Wyss (2005), Variations in earthquake-size distribution across different stress regimes, *Nature*, *437*, 539–542.

Shearer, P., E. Hauksson, and G. Lin (2005), Southern California hypocenter relocation with waveform cross-correlation: Part 2. Results using source-specific station terms and cluster analysis, *Bull. Seismol. Soc. Am.*, *95*, 904–915.

Sibson, R. H. (1974), Frictional constraints on thrust, wrench and normal faults, *Nature*, *249*, 542–544.

Sibson, R. H. (1982), Fault zone models, heat flow, and the depth distribution of earthquakes in the continental crust of the United States, *Bull. Seismol. Soc. Am.*, *72*, 151–163.

Sibson, R. H. (1984), Roughness at the base of the seismogenic zone: Contributing factors, *J. Geophys. Res.*, *89*, 5791–5799.

Singh, S. K., and M. Ordaz (1994), Seismic energy release in mexican subduction zone earthquakes, *Bull. Seismol. Soc. Am.*, *84*, 1533–1550.

Snoke, J. A. (1987), Stable determination of (Brune) stress drops, *Bull. Seismol. Soc. Am.*, *77*, 530–538.

Thatcher, W., and T. C. Hanks (1973), Source parameters of southern California earthquakes, *J. Geophys. Res.*, *78*, 8547–8576.

Townend, J., and M. D. Zoback (2001), Implications of earthquake focal mechanisms for the frictional strength of the San Andreas fault system, *Geol. Soc. Spec. Publ.*, *186*, 13–21.

Tse, S. T., and J. R. Rice (1986), Crustal earthquake instability in relation to the depth variation of frictional slip properties, *J. Geophys. Res.*, *91*, 9452–9472.

Tucker, B. E., and J. N. Brune (1973), Seismograms, *S*-wave spectra and source parameters for aftershocks of the San Fernando earthquake of February 9, 1971, special report, NOAA, Boulder, Colo.

Wald, D. J., and T. H. Heaton (1994), Spatial and temporal distribution of slip for the 1992 Landers, California, earthquake, *Bull. Seismol. Soc. Am.*, *84*, 668–691.

Warren, L. M., and P. M. Shearer (2000), Investigating the frequency dependance of mantle *Q* by stacking *P* and *PP* spectra, *J. Geophys. Res.*, *105*, 25,391–25,402.

Warren, L. M., and P. M. Shearer (2002), Mapping lateral variations in upper mantle attenuation by stacking P and PP spectra, *J. Geophys. Res.*, *107*(B12), 2342, doi:10.1029/2001JB001195.

Wiemer, S., and M. Wyss (2002), Mapping spatial variability of the frequency-magnitude distribution of earthquakes, *Adv. Geophys.*, *45*, 259–302.

Wu, H., and J. M. Lees (1996), Attenuation structure of Coso Geothermal area, California, from wave pulse widths, *Bull. Seismol. Soc. Am.*, *86*, 1574–1590.

Wyss, M. (1973), Towards a physical understanding of the earthquake frequency distribution, *Geophys. J.R. Astron. Soc.*, *31*, 341–359.

Wyss, M., and J. N. Brune (1971), Regional variations of source properties in southern California estimated from the ratio of short- to long-period amplitudes, *Bull. Seismol. Soc. Am.*, *61*, 1153–1167.

Young, C.-Y., and R. W. Ward (1980), Three-dimensional Q^{-1} model of the Coso Hot Springs known geothermal area, *J. Geophys. Res.*, *85*, 2459–2470.

Zhuo, Y., and H. Kanamori (1987), Regional variation of the short-period (1 to 10 second) source spectrum, *Bull. Seismol. Soc. Am.*, *77*, 514–529.

Zoback, M. D., et al. (1987), New evidence on the state of stress of the San Andreas fault system, *Science*, *238*, 1105–1111.

E. Hauksson, Seismological Laboratory, California Institute of Technology, MS 252-21 1200 East California Blvd., Pasadena, CA 91125, USA.

G. A. Prieto and P. M. Shearer, Institute of Geophysics and Planetary Physics, Scripps Institution of Oceanography, University of California, San Diego, 9500 Gilman Drive, Mail Code 0225, La Jolla, CA 92093-0225, USA. (pshearer@ucsd.edu)